Available online at www.sciencedirect.com
ScienceDirect
Acta Materialia 56 (2008) 3422–3438
Acta MATERIALIA
www.elsevier.com/locate/actamat

Effects of solute concentrations on kinetic pathways in Ni–Al–Cr alloys

Christopher Booth-Morrison [a], Jessica Weninger [a], Chantal K. Sudbrack [a], Zugang Mao [a], Ronald D. Noebe [b], David N. Seidman [a,c,*]

[a] Department of Materials Science and Engineering, Northwestern University, 2220 Campus Drive, Evanston, IL 60208-3108, USA
[b] NASA Glenn Research Center, 21000 Brookpark Road, Cleveland, OH 44135, USA
[c] Northwestern University Center for Atom-Probe Tomography (NUCAPT), 2220 Campus Drive, Evanston, IL 60208-3108, USA

Received 13 December 2007; received in revised form 5 March 2008; accepted 16 March 2008
Available online 20 April 2008

Abstract

The kinetic pathways resulting from the formation of coherent γ'-precipitates from the γ-matrix are studied for two Ni–Al–Cr alloys with similar γ'-precipitate volume fractions at 873 K. The details of the phase decompositions of Ni–7.5Al–8.5Cr at.% and Ni–5.2Al–14.2Cr at.% for aging times from 1/6 to 1024 h are investigated by atom-probe tomography, and are found to differ significantly from a mean-field description of coarsening. The morphologies of the γ'-precipitates of the alloys are similar, though the degrees of γ'-precipitate coagulation and coalescence differ. Quantification within the framework of classical nucleation theory reveals that differences in the chemical driving forces for phase decomposition result in differences in the nucleation behavior of the two alloys. The temporal evolution of the γ'-precipitate average radii and the γ-matrix supersaturations follow the predictions of classical coarsening models. The compositional trajectories of the γ-matrix phases of the alloys are found to follow approximately the equilibrium tie-lines, while the trajectories of the γ'-precipitates do not, resulting in significant differences in the partitioning ratios of the solute elements.

Keywords: Nickel-based superalloys; Atom-probe tomography; Temporal evolution; Nanostructures

1. Introduction

The high temperature strength and creep resistance of modern nickel-based superalloys are due to the presence of coherent, elastically hard, $L1_2$-ordered γ'-precipitates in a γ (fcc) nickel-rich solid-solution matrix [1,2]. Efforts to improve these properties by process optimization and to develop reliable life-prediction techniques have created a demand for a quantitative understanding of the kinetic pathways that lead to phase decomposition at service temperatures up to 1373 K [3,4]. The technological importance of commercial nickel-based superalloys has motivated extensive investigations of the precipitation of the γ'-phase from the supersaturated γ-matrix of model alloys by conventional [5–9] and high-resolution [10] transmission electron microscopy (TEM), X-ray analysis [11–13], small-angle and wide-angle neutron scattering [14–17], atom-probe field-ion microscopy [18–21], atom-probe tomography (APT) [22–24], and phase field modeling [25–30]. Many of these techniques are limited by either, or both, their spatial and analytical resolutions for composition [31], and thus the early stages of phase decomposition are still not well understood. This is particularly true of concentrated multicomponent alloys, due, in part, to the complexity of the diffusion processes involved [32].

The research of Schmuck et al. [22,33] and Pareige et al. [34,35] combined APT and lattice kinetic Monte Carlo (LKMC) simulation to analyze the decomposition of an Ni–Al–Cr solid-solution. A similar approach was applied by Sudbrack et al. [36–40] and Yoon et al. [41–43] for studying Ni–5.2Al–14.2Cr at.% aged at 873 K and Ni–10Al–8.5Cr at.%, Ni–10Al–8.5Cr–2.0W at.% and Ni–10Al–8.5Cr–2.0Re at.% aged at 1073 K, which decompose

* Corresponding author. Address: Department of Materials Science and Engineering, Northwestern University, 2220 Campus Drive, Evanston, IL 60208-3108, USA. Tel.: +1 847 491 4391; fax: +1 847 467 2269.
E-mail address: d-seidman@northwestern.edu (D.N. Seidman).

1359-6454/$34.00
doi:10.1016/j.actamat.2008.03.016

via a first order phase transformation to form a high number density, $N_v(t)$, of nanometer-sized γ'-precipitates ($\sim 10^{20}$ to 10^{25} m^{-3}). The addition of Cr to the binary Ni–Al system reduces the lattice parameter misfit between the γ'-$Ni_3(Al_xCr_{1-x})$ precipitates and the γ-matrix, often leading to γ'-precipitates that are nearly misfit free [6], thereby allowing the γ'-precipitates to remain spheroidal to fairly large dimensions as aging progresses [11]. At 873 K, γ'-precipitate radii as large as ~10 nm are measured by APT for concentrated Ni–Al–Cr alloys [37]. The formation of coherent, spheroidal γ'-precipitates with relatively stress-free precipitate/matrix heterophase interfaces in the model Ni–Al–Cr alloys studied herein makes them excellent candidates for comparison of experimental data with the predictions of classical treatments of nucleation, growth and coarsening for ternary alloys, for which there is very little detailed quantitative experimental data available.

The present investigation focuses on comparing the temporal evolution of the nanostructural and compositional properties at 873 K of alloy (A), Ni–7.5Al–8.5Cr at.%, with those previously reported for alloy (B), Ni–5.2Al–14.2Cr at.% [36,37,40]; all concentrations herein are in at.% unless otherwise noted. A ternary Ni–Al–Cr phase diagram determined by the Grand Canonical Monte Carlo (GCMC) technique at 873 K (Fig. 1 [44]) predicts that the values of the equilibrium volume fractions of the γ'-phase, ϕ^{eq}, are 17.5 ± 0.5 and 15.1 ± 0.5 for alloys (A) and (B), respectively. Since the values of ϕ^{eq} for alloys (A) and (B) are similar, it follows that any differences observed in the kinetic pathways during decomposition are principally due to differences in solute concentrations.

1.1. Classical nucleation theory

The early stages of phase decomposition by nucleation have been studied theoretically in a set of models known as classical nucleation theory (CNT), which have been reviewed extensively in the literature [31,45–48]. According to CNT, nucleation is governed by a balance between a bulk free energy term, which has both chemical, ΔF_{ch}, and elastic strain energy, ΔF_{el}, components, and an interfacial free energy term, $\sigma^{\gamma/\gamma'}$, associated with the formation of a γ-matrix/γ'-precipitate heterophase interface; F is the Helmholtz free energy. Thus, the expression for the net reversible work required for the formation of a spherical nucleus, W_R, as a function of nucleus radius, R, is given by

$$W_R = (\Delta F_{ch} + \Delta F_{el})\frac{4\pi}{3}R^3 + 4\pi R^2\sigma^{\gamma/\gamma'}. \quad (1)$$

According to CNT, the net reversible work acts as a nucleation barrier that nuclei must surmount to achieve a critical nucleus radius, R^*. The critical net reversible work, W_R^*, required for the formation of a critical spherical nucleus is expressed as

$$W_R^* = \frac{16\pi}{3}\frac{(\sigma^{\gamma/\gamma'})^3}{(\Delta F_{ch} + \Delta F_{el})^2} \quad (2)$$

and R^* is given by

$$R^* = \frac{2\sigma^{\gamma/\gamma'}}{-(\Delta F_{ch} + \Delta F_{el})}. \quad (3)$$

For nucleation to occur, $(\Delta F_{ch} + \Delta F_{el})$ must be negative. From CNT, the stationary-state nucleation current, J^{st}, which is the number of nuclei formed per unit time per unit volume, is given by

$$J^{st} = Z\beta^* N_0 \exp\left(\frac{-W_R^*}{k_B T}\right), \quad (4)$$

where Z, the Zeldovich factor, accounts for the dissolution of supercritical clusters, β is a kinetic coefficient describing the rate of condensation of single atoms on the critical nuclei, N_0 is the total number of possible nucleation sites per unit volume, taken to be the volume density of lattice sites occupied by Al, the precipitate-forming solute [49,50], k_B is Boltzmann's constant and T is the absolute temperature in degrees Kelvin. In their review of nucleation kinetics results for binary alloys, Aaronson and Legoues [51] note that while there exists some experimental evidence to support the correctness of CNT, the nucleation currents predicted by the extant theories are often several orders of magnitude smaller than those measured experimentally, which is most likely due to the presence of precursor clusters that form between the solutionizing, and quenching and aging treatments. Such precursor clustering has been detected in both alloys (A) [36] and (B), and thus it is anticipated that our calculated values of J^{st} will be smaller than those measured by APT.

1.2. Coarsening theory

The first comprehensive mean-field treatment of Ostwald ripening [52], due to Lifshitz and Slyozov [53] and Wagner [54], known as the LSW model, is limited to dilute binary alloys with spatially fixed spherical precipitates whose initial compositions are equal to their equilibrium values. The LSW model for a binary alloy assumes: (i) no elastic interactions among precipitates, thereby limiting the precipitate volume fraction to zero; (ii) precipitates have a spherical morphology; (iii) coarsening occurs in a stress-free matrix; (iv) the precipitate diffusion fields do not overlap; (v) dilute solid-solution theory obtains; (vi) the linearized version of the Gibbs–Thomson equation is valid; (vii) coarsening occurs by the evaporation–condensation mechanism; and (viii) precipitates coarsen with a fixed chemical composition, which is the equilibrium composition. These requirements are highly restrictive and difficult to meet in practice, and while experimental evidence exists to support the prediction of the time dependency of the mean precipitate radius, $\langle R(t)\rangle$, experimentalists have been unable to achieve the exact stationary-state precipitate size distributions predicted by the LSW model [3,55,56]. Researchers have worked to remove the mean-field restrictions by developing models based on multiparticle diffusion

that are able to describe stress-free systems with finite volume fractions [55,57,58].

Umantsev and Olson (UO) [59] were the first to demonstrate that the exponents of the temporal power laws predicted for binary alloys by LSW-type models are identical for concentrated multi-component alloys, but that the explicit expressions for the rate constants depend on the number of components. The UO model did not allow the composition of the precipitates to evolve temporally, which is also true for the Morral and Purdy treatment [60]. Kuehmann and Voorhees (KV) [61] considered isothermal quasi-stationary state coarsening in ternary alloys and developed a model that permits the precipitate composition to evolve, such that the matrix and precipitate compositions can deviate locally from their equilibrium thermodynamic values. In the quasi-stationary limit in the KV model, $\delta C_i/\delta t \approx 0$, the exponents of the power-law temporal dependencies for $\langle R(t)\rangle$, $N_v(t)$ and the γ-matrix supersaturation, $\Delta C_i^{\gamma}(t)$, of each solute species i are

$$\langle R(t)\rangle^3 - \langle R(t_0)\rangle^3 = K_{\mathrm{KV}}(t - t_0), \tag{5}$$

$$N_v(t)^{-1} - N_v(t_0)^{-1} = \frac{4.74K_{\mathrm{KV}}}{\phi^{\mathrm{eq}}}(t - t_0), \tag{6}$$

$$\Delta C_i^{\gamma}(t) = \langle C_i^{\gamma,ff}(t)\rangle - C_i^{\gamma,\mathrm{eq}}(\infty) = \kappa_{i,\mathrm{KV}}^{\gamma} t^{-1/3}, \tag{7}$$

where K_{KV} and $\kappa_{i,\mathrm{KV}}^{\gamma}$ are the coarsening rate constants for $\langle R(t)\rangle$ and $\Delta C_i^{\gamma}(t)$, respectively, $\langle R(t_0)\rangle$ is the average precipitate radius and $N_v(t_0)$ is the precipitate number density at the *onset* of quasi-stationary coarsening, at time t_0. The quantity $\Delta C_i^{\gamma}(t)$ is denoted a supersaturation and is the difference between the concentration in the far-field γ-matrix, $\langle C_i^{\gamma,ff}(t)\rangle$, and the equilibrium γ-matrix solute-solubility, $C_i^{\gamma,\mathrm{eq}}(\infty)$. The quantity $C_i^{\gamma,\mathrm{eq}}(\infty)$ needs to be calculated or determined experimentally as it is not available for Ni–Al–Cr multicomponent alloys at 873 K.

APT of the nanostructures of alloys (A) and (B) provides an in-depth examination of the compositional and nanostructural evolution of the γ'-precipitate phase as it evolves toward its equilibrium thermodynamic composition. In this article, the decomposition of the γ-matrix phase, from the earliest stages of solute-rich γ'-nuclei formation to the subsequent growth and coarsening of γ'-precipitates, is accessed within the framework of classical nucleation, growth and coarsening theories. The effects of varying the solute concentrations on the temporal evolution of the Ni–Al–Cr alloys are shown to provide a quantitative understanding of the kinetic pathways that lead to phase separation, and the achievement of the equilibrium compositions of both phases. We demonstrate that the kinetic pathways to achieve thermodynamic equilibrium for the two alloys are very different, even though the equilibrium volume fractions of the γ'-phase are approximately equal.

2. Experimental

High-purity constituent elements (99.97 wt.% Ni, 99.98 wt.% Al and 99.99 wt.% Cr) were induction-melted and chill cast in a 19 mm diameter copper mold under an Ar atmosphere. The overall compositions of the two alloys were determined by inductively coupled plasma atomic-emission spectroscopy, which yielded average atomic compositions of 83.87Ni–7.56Al–8.56Cr and 80.52Ni–5.24Al–14.24Cr for alloys (A) and (B), respectively. Chemical homogeneity of the cast ingots was achieved by annealing at 1573 K in the γ-phase field for 20 h. Next, the ingots were held in the γ-phase field at 1123 K for 3 h to reduce the concentration of quenched-in vacancies, and then water quenched and sectioned. Ingot sections were then aged at 873 K under flowing argon for times ranging from 1/6 to 1024 h and water quenched, and microtip specimens were prepared from each of the aged sections for study by APT. We performed voltage-pulsed APT with a conventional APT [62,63] and an Imago Scientific Instrument's local-electrode atom-probe (LEAP™) tomograph [64–67]. APT data collection was performed at a specimen temperature of 40.0 ± 0.3 K, a voltage pulse fraction (pulse voltage/steady-state direct current voltage) of 19%, a pulse frequency of 1.5 kHz (conventional APT) or 200 kHz (LEAP™ tomograph), and a background gauge pressure of $<6.7 \times 10^{-8}$ Pa. The average detection rate in the area of analysis ranged from 0.011 to 0.015 ions per pulse for conventional APT and from 0.04 to 0.08 ions per pulse for the LEAP™ tomographic analyses. Conventional APT data were visualized and analyzed with APEX software, the successor of ADAM [68], while LEAP™ data were analyzed employing the IVAS 3.0 software program (Imago Scientific Instruments, Madison, WI). The γ/γ' interfaces were delineated with 10.5 and 9 at.% Al isoconcentration surfaces generated with efficient sampling procedures [69], for alloys (A) and (B), respectively, and in-depth compositional information was obtained with the proximity histogram method [70]. The volume fraction of the γ'-precipitate phase was defined as the ratio of the total number of atoms contained within the isoconcentration surfaces to the total number of atoms collected. Further experimental and analytical details for alloy (B) can be found elsewhere [37,40]; the same procedures were employed for alloy (A). It is noted that spatial convolution effects such as ion trajectory overlap and local magnification effects have been cited as possible sources of misleading results in APT analysis of nickel-based superalloys [71]. Ion trajectory overlap may cause both interfacial broadening and artificially low values of the γ'-precipitate Al composition, particularly at early aging times. A comparison of the composition profiles across the γ/γ' interfaces measured by APT and simulated by lattice kinetic Monte Carlo simulations for alloy (B) [32] showed no evidence of artificial interfacial broadening in the APT data. Additionally, our results indicate that the Al composition is largest at the shortest aging times due to a supersaturation of Al in the γ'-precipitates, thus trajectory overlap effects are assumed to be minimal for the APT conditions used herein. Local magnification effects due to differences in the required evaporation fields of different phases are not present in

Ni–Al–Cr superalloys containing only γ-matrix and γ-precipitate phases because the evaporation fields of the two phases are essentially identical.

The commercial software package Thermo-Calc [72] was used to calculate the values of ϕ^{eq}, $C_i^{\gamma,eq}(\infty)$ and the equilibrium γ'-precipitate composition of each solute species i, $C_i^{\gamma',eq}(\infty)$, for Ni–7.5Al–8.5Cr and Ni–5.2Al–14.2Cr at a pressure of 1 atm, using databases for nickel-based superalloys from Saunders [73] and Dupin et al. [74]. For comparative purposes, the equilibrium phase boundaries determined by Thermo-Calc using the Saunders and Dupin et al. databases are superimposed on the GCMC phase diagram at 873 K (Fig. 1). While the generated $\gamma/\gamma+\gamma'$ solvus lines show good agreement, the curvatures of the $\gamma+\gamma'/\gamma'$ phase lines differ for each technique. Although the Ni–Al–Cr system was studied extensively by Taylor and Floyd [6], there is no extant experimental phase diagram at 873 K for comparison.

3. Results

3.1. Morphological development

Nanometer-sized spheroidal γ'-precipitates are detected in alloys (A) and (B) over the full range of aging times, from 1/6 to 1024 h. The temporal evolution of the morphology of alloy (A) is shown in a series of APT micrographs in Fig. 2, which can be compared with a similar series for alloy (B) in Ref. [37]. Fig. 3 is a projection of a $25 \times 25 \times 25\ nm^3$ subset of an APT analysis of alloy (A) aged to 1024 h, showing a spheroidal γ'-precipitate with a radius of ~9 nm, delineated by a dark 10.5% Al isoconcentration surface. Atomic planes are clearly visible within the γ'-precipitate, and the value of the interplanar spacing is 0.26 ± 0.03 nm, suggesting {1 1 0}-type planes. This APT image demonstrates that the γ'-precipitates remain spheroidal for aging times as long as 1024 h at an aging temperature of 873 K, as confirmed by the TEM micrograph in Fig. 4.

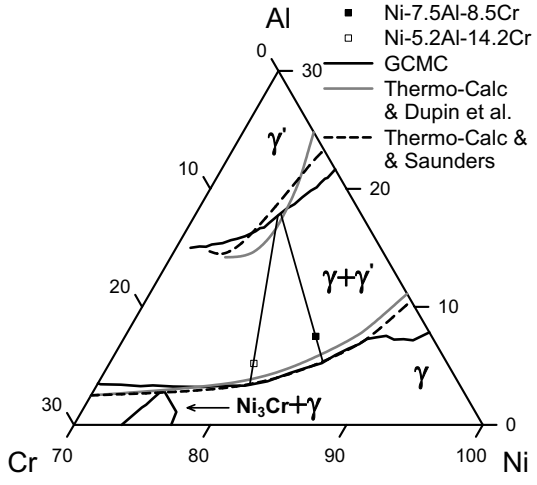

Fig. 1. A partial ternary phase diagram of the Ni–Al–Cr system at 873 K calculated using the GCMC simulation technique [44], showing the proximity of both alloys (A), Ni–7.5Al–8.5Cr, and (B), Ni–5.2Al–14.2Cr, to the $(\gamma+\gamma')/\gamma$ solvus line. The tie-lines are drawn through the nominal compositions of the alloys and between the equilibrium phase compositions determined by extrapolation of APT concentration data to infinite time. Equilibrium solvus curves determined by Thermo-Calc [97], using databases for nickel-based superalloys due to Saunders [73] and Dupin et al. [74], are superimposed on the GCMC phase diagram for comparative purposes.

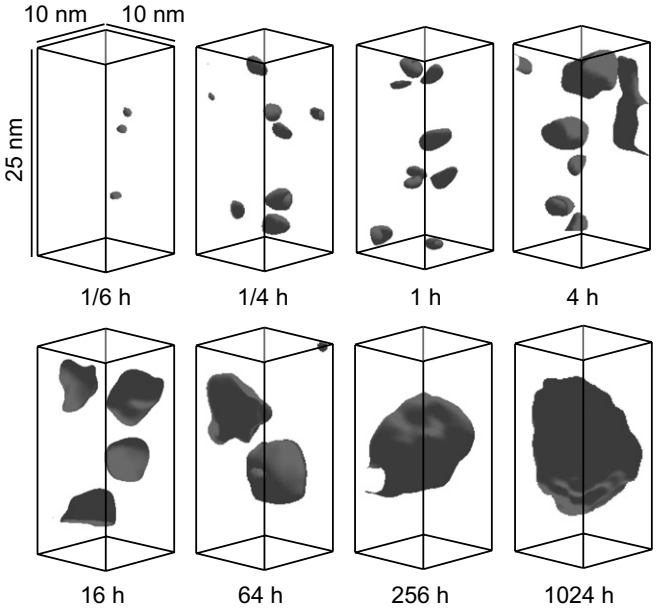

Fig. 2. The temporal evolution of the γ'-precipitate nanostructure in Ni–7.5Al–8.5Cr aged at 873 K is displayed in a series of APT parallelepipeds. The parallelepipeds are $10 \times 10 \times 25\ nm^3$ subsets of the analyzed volume and contain ~125,000 atoms. The γ/γ' interfaces are delineated in gray with 10.5% Al isoconcentration surfaces.

There is evidence of γ'-precipitate coagulation and coalescence in alloys (A) and (B), characterized by the formation of necks that interconnect the γ'-precipitates and exhibit $L1_2$-type ordering. Although the first γ'-nuclei are detected by APT at an aging time of 1/6 h, interconnected γ'-precipitates first evolve in both alloys after 1/4 h of aging, which coincides with the end of the quasi-stationary-state nucleation regime. After 1/4 h of aging, the fraction of coagulating and coalescing γ'-precipitates, f, is 15 ± 4 and $9 \pm 3\%$ for alloys (A) and (B), respectively. From Fig. 5, the maximum value of f of $18 \pm 4\%$ for alloy (A) occurs at an aging time of 1 h, while the maximum value for alloy (B) of $30 \pm 4\%$ occurs at an aging time of 4 h.

3.2. Temporal evolution of the nanostructural properties of γ'-precipitates

Fig. 6 provides a quantitative description of the temporal evolution of the γ'-precipitate volume fraction, ϕ, and the quantities $\langle R(t)\rangle$ and $N_v(t)$ for alloys (A) and (B). The γ'-precipitate nanostructural properties determined by APT analysis for alloy (A) are summarized in Table 1,

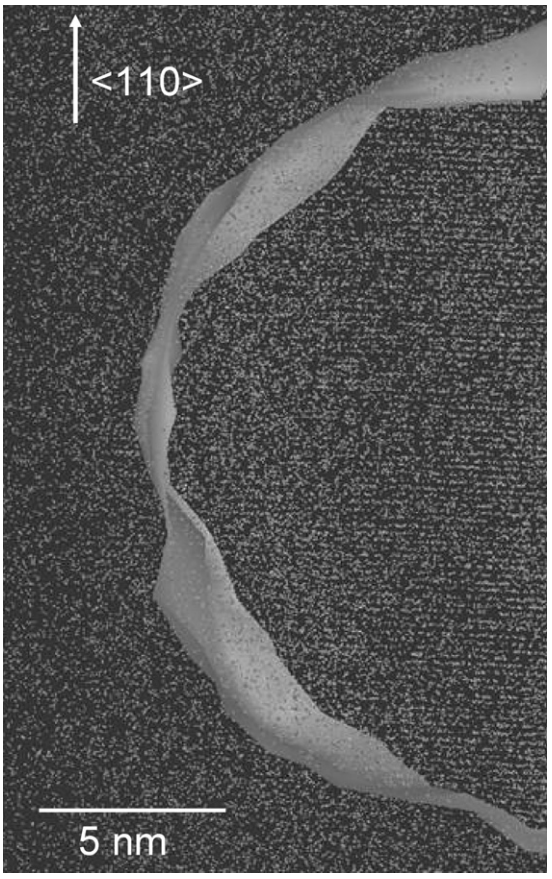

Fig. 3. A subset of an APT micrograph of Ni–7.5Al–8.5Cr aged at 873 K for 1024 h, containing 350,000 atoms, with the Ni and Cr atoms omitted for clarity. A γ'-precipitate with a radius of $\sim$9 nm is delineated by the dark 10.5% Al isoconcentration surface, and shows {1 1 0}-type superlattice planes with an interplanar spacing of 0.26 ± 0.03 nm.

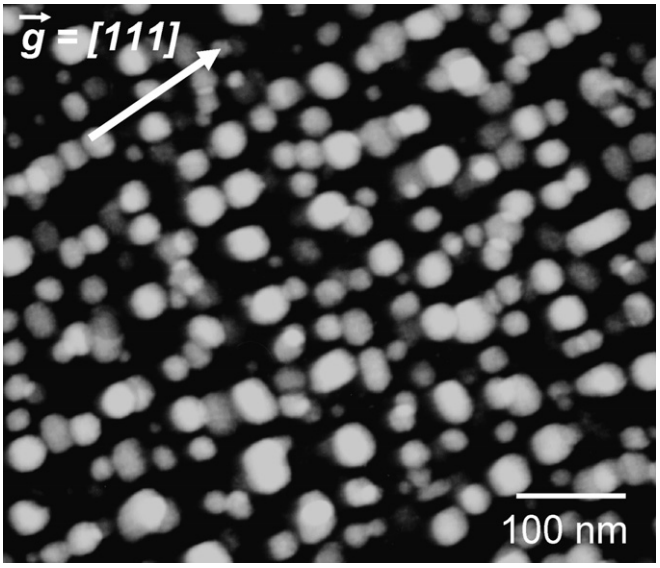

Fig. 4. A centered superlattice reflection dark–field image of spheroidal $Ni_3(Al_xCr_{(1-x)})\gamma'$-precipitates for a Ni–7.5Al–8.5Cr sample aged for 1024 h at 873 K. Image recorded near the [0 1 1] zone axis, and $\mathbf{g} = [1\,1\,1]$ is the operating reflection.

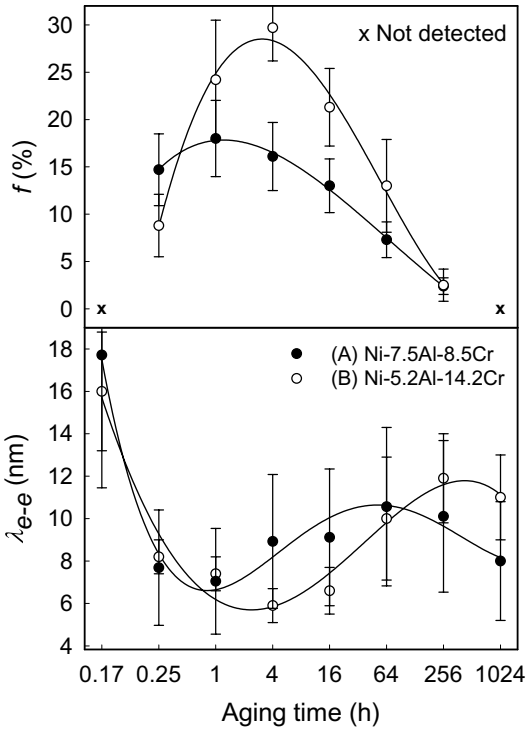

Fig. 5. The temporal evolution of the value of the fraction of γ'-precipitates interconnected by necks, f, and the average interprecipitate edge-to-edge spacing, $\langle\lambda_{e-e}\rangle$. The maximum value of f is $18 \pm 4\%$, corresponding to the minimum value of $\langle\lambda_{e-e}\rangle$ of 7 ± 2 nm at an aging time of 1 h for alloy (A), Ni–7.5Al–8.5Cr. For alloy (B), Ni–5.2Al–14.2Cr, the minimum value of $\langle\lambda_{e-e}\rangle$ of 5.9 ± 0.8 nm and the maximum value of f of $30 \pm 4\%$ coincide at an aging time of 4 h.

while Ref. [37] contains details for alloy (B). The standard errors for all quantities, σ, are calculated based on counting statistics and reconstruction scaling errors using standard error propagation methods [75], and represent one standard deviation from the mean. The two Ni–Al–Cr alloys were designed to have similar values of ϕ^{eq} of $\sim$16%, and the measured values of ϕ for alloy (A) and (B) are statistically indistinguishable over the full range of aging times, from 1/6 to 1024 h. It is worth noting that, over the range of aging times studied, the values of $\langle R(t)\rangle$ of alloy (A) are, on average, $32 \pm 6\%$ larger than those of alloy (B). From Fig. 6, the temporal evolution of alloys (A) and (B) can be divided into three regimes: (i) quasi-stationary-state γ'-precipitate nucleation at early aging times; followed by (ii) concomitant precipitate nucleation and growth; and finally (iii) concurrent growth and coarsening once the maximum value of $N_v(t)$ is achieved. The characteristic microstructural evolution associated with these three regimes is described in detail below.

3.2.1. Nucleation and growth of γ'-precipitates

Phase decomposition in alloys (A) and (B) begins with the formation of solute-rich nuclei that grow to form stable γ'-precipitates. Precipitates are first detected by APT in alloys (A) and (B) after 1/6 h of aging. Alloy (A) forms $(2.6 \pm 1.4) \times 10^{23}$ γ'-precipitates m^{-3} with an

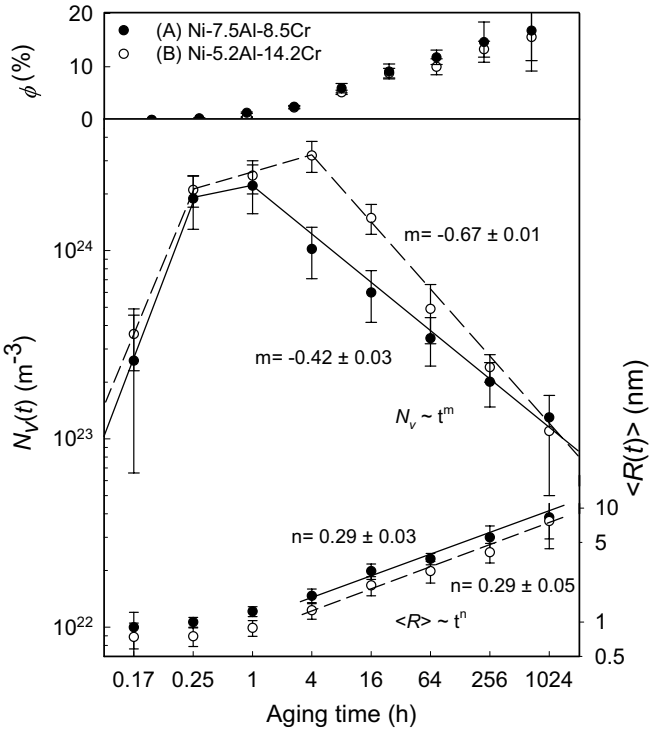

Fig. 6. The temporal evolution of the γ'-precipitate volume fraction, ϕ, number density, $N_v(t)$, and mean radius, $\langle R(t)\rangle$, for (A) Ni–7.5Al–8.5Cr and (B) Ni–5.2Al–14.2Cr alloys aged at 873 K as determined by APT microscopy. The quantity $\langle R(t)\rangle$ is proportional to $t^{1/3}$ as predicted by the UO and KV models for isothermal coarsening in ternary alloys. The temporal dependence of the diminution of the quantity $N_v(t)$ deviates from the t^{-1} prediction of the UO and KV models for both alloys.

$\langle R(t = 1/6\text{ h})\rangle$ value of 0.90 ± 0.32 nm, corresponding to a ϕ value of $0.31 \pm 0.11\%$, after 1/6 h of aging. For the same aging time, alloy (B) forms $(3.6 \pm 1.3) \times 10^{23}$ γ'-precipitates m^{-3} with an $\langle R(t = 1/6\text{ h})\rangle$ value of 0.74 ± 0.24 nm, accounting for a ϕ value of $0.11 \pm 0.04\%$. The nucleation of stable γ'-precipitates in alloy (A) for aging times between 1/6 and 1/4 h results in a sharp linear slope of the $N_v(t)$ profile of $(5.4 \pm 1.5) \times 10^{21}$ m^{-3} s^{-1}, while the values of $\langle R(t)\rangle$ of 0.90 ± 0.32 and 1.00 ± 0.11 nm remain constant within statistical error. This slope for $N_v(t)$, although based on two experimental data points, is taken to be an estimate of the quasi-stationary-state nucleation current of γ'-precipitates, J^{st}. In contrast, alloy (B) undergoes nucleation of stable γ'-precipitates with a constant $\langle R(t)\rangle$ value of 0.75 ± 0.24 nm for aging times less than 1/4 h. The value of J^{st} for alloy (B) is estimated to be $(5.9 \pm 1.7) \times 10^{21}$ m^{-3} s^{-1}, which is statistically indistinguishable from the value of J^{st} of $(5.4 \pm 1.5) \times 10^{21}$ m^{-3} s^{-1} measured for alloy (A).

At an aging time of 1/4 h, alloys (A) and (B) enter a regime of concomitant γ'-precipitate nucleation and growth, which results in steadily increasing ϕ and $\langle R(t)\rangle$ values, and a maximum value for $N_v(t)$. The peak value in $N_v(t)$ of $(2.21 \pm 0.64) \times 10^{24}$ m^{-3} for alloy (A) occurs at 1 h, while for alloy (B), the peak value in $N_v(t)$ of $(3.2 \pm 0.6) \times 10^{24}$ m^{-3} is achieved at 4 h. We note that the prediction of the temporal dependence of $\langle R(t)\rangle$ of $t^{1/2}$ for diffusion-limited growth [76–78] is *not* observed in either of the Ni–Al–Cr alloys studied, contrary to the results for an earlier APT study of an alloy whose composition is essentially identical to that of alloy (B) [22].

3.2.2. Growth and coarsening of γ'-precipitates

Beyond the peak in $N_v(t)$, alloys (A) and (B) enter a quasi-stationary state of growth and coarsening characterized by a steady diminution of $N_v(t)$ and increasing values of ϕ and $\langle R(t)\rangle$. Beyond 1 h, the quantity $N_v(t)$ for alloy (A) displays a temporal dependence of $t^{-0.42\pm0.03}$, which differs significantly from the predicted value of t^{-1} from the UO and KV models. This is not surprising, since the quantity ϕ continues to evolve temporally in this regime, implying that the system has not achieved a stationary state [79]. During coarsening in alloy (B), the quantity $N_v(t)$ displays a temporal dependence of $t^{-0.67\pm0.01}$ beyond an aging time of 4 h, which also differs from the predicted value of t^{-1}, though to a lesser extent. The values of ϕ for the two alloys increase steadily in this regime, reaching values of ϕ of $16.0 \pm 5.7\%$ and $15.6 \pm 6.4\%$ for alloys (A) and (B), respectively, which are statistically indistinguishable. In the

Table 1
Temporal evolution of the nanostructural properties of γ'-precipitates[a] determined by APT for Ni–7.5Al–8.5Cr aged at 873 K

Aging time (h)	N_{ppt}[b]	$\langle R(t)\rangle \pm \sigma$ (nm)	$N_v(t) \pm \sigma$ ($\times 10^{24}$ m^{-3})	$\phi \pm \sigma$ (%)	$f \pm \sigma$ (%)	$\langle \lambda_{e-e}\rangle \pm \sigma$ (nm)
1/6	8	0.90 ± 0.32	0.26 ± 0.14	0.31 ± 0.11	ND[c]	17.7 ± 6.3
1/4	101	1.00 ± 0.11	1.89 ± 0.59	1.36 ± 0.14	15 ± 4	7.7 ± 2.7
1	70.5	1.24 ± 0.12	2.21 ± 0.64	2.48 ± 0.25	18 ± 4	7.0 ± 2.5
4	46	1.70 ± 0.25	1.02 ± 0.31	5.98 ± 0.88	16 ± 3	8.9 ± 3.2
16	42	2.80 ± 0.43	0.60 ± 0.18	9.12 ± 1.4	13 ± 3	9.1 ± 3.2
64	76.5	3.59 ± 0.41	0.34 ± 0.10	11.8 ± 1.4	7.4 ± 1.9	10.6 ± 3.7
256	15	5.54 ± 1.43	0.20 ± 0.05	14.6 ± 3.8	2.5 ± 0.9	10.1 ± 3.6
1024	8	8.30 ± 2.93	0.13 ± 0.05	16.0 ± 5.7	ND[c]	7.9 ± 2.8

[a] Mean radius of γ'-precipitates, $\langle R(t)\rangle$; the number density, $N_v(t)$; precipitated volume fraction, ϕ; fraction of γ'-precipitates interconnected by necks, f; average edge-to-edge interprecipitate spacing, $\langle \lambda_{e-e}\rangle$; and their standard errors, σ. One standard deviation is reported.

[b] The number of γ'-precipitates analyzed, N_{ppt}, is smaller than the total number of γ'-precipitates detected by APT. Precipitates that intersect the sample volume contribute 0.5 to the quantity N_{ppt}, and are included in the estimates of $N_v(t)$, ϕ, f and the phase compositions, but not in the measurement of $\langle R(t)\rangle$.

[c] ND, not detected.

growth and coarsening regime, the quantity $\langle R(t)\rangle$ displays a temporal dependence of $t^{0.29\pm0.03}$ for alloy (A) and $t^{0.29\pm0.05}$ for alloy (B), which both agree approximately, but not exactly, with the predicted value of $t^{1/3}$, indicating that the phase transformation is primarily diffusion-limited.

From Fig. 5, the maximum value for f, after 1 h of aging, of $18 \pm 4\%$ for alloy (A) coincides with the minimum value of the average edge-to-edge interprecipitate spacing, $\langle\lambda_{e\text{–}e}\rangle$, of 7.0 ± 2.5 nm and the peak value of $N_v(t)$ of $(2.21 \pm 0.64) \times 10^{24}$ m^{-3}. For alloy (B), the peak value of $N_v(t)$, at an aging time of 4 h, is $(3.2 \pm 0.6) \times 10^{24}$ m^{-3}, corresponding to a minimum value of $\langle\lambda_{e\text{–}e}\rangle$ of 5.9 ± 0.8 nm at a maximum value of f of $30 \pm 4\%$. The quantity $\langle\lambda_{e\text{–}e}\rangle$ is calculated using Eq. (8), which assumes (i) a regular simple cubic array of γ'-precipitates; and (ii) the unit volume is equivalent to that of a lattice enclosed sphere in order to preserve the radial symmetry of the three-dimensional structure [37]:

$$\langle\lambda_{e-e}\rangle = 2\left[\left(\frac{4}{3}\pi \cdot N_v(t)\right)^{-1/3} - \langle R(t)\rangle\right]. \tag{8}$$

3.3. Temporal evolution of the compositions of the γ and γ'-phases

The compositions of the γ-matrix and the γ'-precipitate phases of alloys (A) and (B) evolve temporally as the γ-matrix becomes enriched in Ni and Cr and depleted in Al, as shown in Fig. 7 for alloy (A). The compositional trajectories of the γ-matrix and γ'-precipitate phases are shown on a partial Ni–Al–Cr ternary phase diagram at 873 K in Fig. 8. The mean-field KV model of quasi-stationary state coarsening predicts that the slope of the trajectory of the γ-matrix phase during coarsening lies along the equilibrium tie-line and has a value of p_{Al}/p_{cr}, where p_i is the magnitude of the partitioning of solute species i, defined as $p_i = [C_i^{\gamma',eq}(\infty) - C_i^{\gamma,eq}(\infty)]$. For a binary alloy, the compositions at the interface are given by the assumption of local equilibrium, whereas for a ternary alloy, the interfacial compositions must be further defined by the condition of flux balance at the interface [57]. As such, according to the KV model, the addition of a third alloying element alters both the form of the Gibbs–Thompson equations and the predictions of the temporal evolution of the phase compositions. The compositional trajectory of the γ'-precipitate phase is predicted to lie on a straight line that is not necessarily parallel to the equilibrium tie-line, which is the case for both alloys (A) and (B). In order to quantify deviations from the equilibrium tie-line, the quantities $\delta C_{Al}^{\gamma}(t)/\delta C_{Cr}^{\gamma}(t)$ and $\delta C_{Al}^{\gamma'}(t)/\delta C_{Cr}^{\gamma'}(t)$ for aging times of 4–1024 h are compared to the values of p_{Al}/p_{cr} for both alloys. The trajectories of the γ-matrix phase and the γ'-precipitate phase compositions of alloy (A) have slopes of -2.56 ± 0.12 and 2.86 ± 0.32, respectively, while the slope of the equilibrium tie-line is estimated to be -3.52 ± 0.09. Slopes of -1.10 ± 0.29 and 1.21 ± 0.34 are estimated for the γ-matrix and γ'-precipitate phases, respectively, from the APT data for alloy (B), while the slope of the equilibrium tie-line is -1.53 ± 0.07. From these results, it is absolutely clear that the trajectories of the composition of the γ'-precipitate phases in alloys (A) and (B) do *not* lie along the equilibrium tie-line of the respective alloys, which is contrary to all coarsening models except the KV model. The trajectories of the composition of the γ-matrix phase of alloys (A) and (B) lie approximately along the tie-lines, although the magnitude of the slope of the experimental compositional trajectory is 27% smaller than that predicted by the mean-field KV model for alloy (A) and is 28% smaller than the predicted slope for alloy (B). Hence, our results indicate that the temporal evolution of ternary alloys is considerably more complicated than for binary alloys, and certainly warrants future research.

During nucleation, solute-rich γ'-nuclei form with large values for the Al and Cr supersaturations. The first γ'-nuclei detected by APT for alloy (A) have solute-supersaturated compositions of 70.9 ± 1.4 Ni, 23.3 ± 1.5 Al and 5.8 ± 0.9 Cr at an $\langle R(t = 1/6\text{ h})\rangle$ value of 0.90 ± 0.32 nm for alloy (A). The γ'-nuclei in alloy (B) have a composition of 71.3 ± 1.6 Ni, 19.1 ± 1.4 Al and 9.7 ± 1.1 Cr, and an $\langle R(t = 1/6\text{ h})\rangle$ value of 0.74 ± 0.24 nm. As phase decomposition progresses beyond nucleation, the magnitude of the values of $\Delta C_i^{\gamma}(t)$ decrease asymptotically toward a value of zero as the equilibrium γ- and γ'-phase compositions are approached. The equilibrium γ-matrix and γ'-precipitate compositions are extrapolated by fitting the measured concentrations from the quasi-stationary coarsening regime to Eq. (7) for aging times beyond 1 h for alloy (A) and 4 h for alloy (B). The equilibrium γ'-precipitate composition of alloy (A) is estimated to be 76.33 ± 0.12 Ni, 17.82 ± 0.15 Al and 5.85 ± 0.12 Cr, while the equilibrium γ-matrix has a composition of 85.19 ± 0.08 Ni, 5.42 ± 0.09 Al and 9.39 ± 0.09 Cr at infinite time. The equilibrium γ'-precipitate phase composition of alloy (B) is estimated to be 76.53 ± 0.25 Ni, 16.69 ± 0.22 Al and 6.77 ± 0.15 Cr, while the equilibrium composition of the γ-matrix phase is 81.26 ± 0.09 Ni, 3.13 ± 0.04 Al and 15.61 ± 0.09 Cr. Summaries of the equilibrium phase compositions of alloy (A) determined by APT are presented in Table 2, and agree with results obtained from Thermo-Calc and GCMC simulation. Ref. [37] contains a similar table for alloy (B).

The partitioning behavior of the elements can be determined quantitatively by calculating the partitioning ratio, $K_i^{\gamma'/\gamma}$, defined as ratio of the concentration of an element i in the γ'-precipitates to the concentration of the same element in the γ-matrix. Fig. 9 demonstrates that alloys (A) and (B) both exhibit partitioning of Al to the γ'-precipitates and of Ni and Cr to the γ-matrix. Partitioning is more pronounced in alloy (B) than (A), as the smaller Al and the larger Cr concentrations of this alloy result in a smaller solubility of Al, and a larger solubility of Cr in the γ-matrix, respectively. Nickel partitions to the γ-matrix with

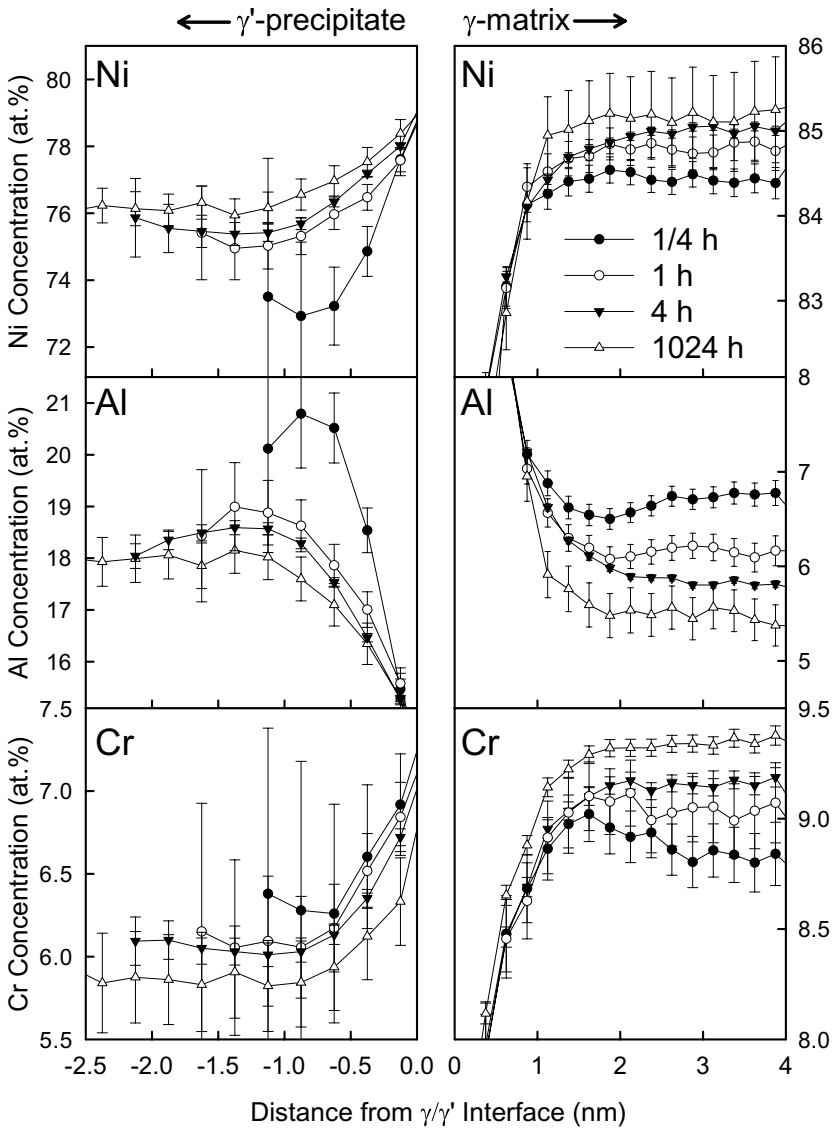

Fig. 7. The composition profiles on either side of the heterophase γ-matrix/γ'-precipitate interface for alloy (A), Ni–7.5Al–8.5Cr, aged at 873 K for aging times of 1/4, 1, 4 and 1024 h. The phase compositions evolve temporally, as the γ-matrix becomes enriched in Ni and Cr and depleted in Al. The values of $\langle R(t)\rangle$ for these aging times are 1.00 ± 0.11 nm for 1/4 h, 1.24 ± 0.12 nm for 1 h, 1.70 ± 0.25 nm for 4 h and 8.30 ± 2.93 nm for 1024 h.

a $K_i^{\gamma'/\gamma}$ of $\sim$0.9 for both alloys, and is only slightly time dependent.

The lever rule is applied to the equilibrium phase compositions for both alloys to estimate a ϕ^{eq} value of $16.4 \pm 0.6\%$ for alloy (A) and $15.7 \pm 0.7\%$ for alloy (B). The ϕ values of 16.0 ± 5.7 and $15.6 \pm 6.4\%$ determined by APT at an aging time of 1024 h for alloys (A) and (B) are within experimental error of the ϕ^{eq} values estimated by the lever rule. The Thermo-Calc software package yields ϕ^{eq} values of 16.7% and 14.9% for alloy (A) according to the Saunders and Dupin et al. databases, respectively, thus the Saunders database yields the value closest to the experimental value of $16.4 \pm 0.6\%$. Alloy (B) is predicted to achieve ϕ^{eq} values of 12.83% and 12.34% for the same databases, which are both smaller than the experimentally determined value of $15.7 \pm 0.7\%$. Summaries of the ϕ^{eq} values determined by APT are presented in Table 3, and agree with results obtained from Thermo-Calc and GCMC modeling to different degrees.

The values of the solid-solution supersaturations of alloys (A) and (B) are calculated based on the equilibrium phase compositions from APT data. The initial solid-solution supersaturation values are estimated to be 2.08 ± 0.02 Al and -0.89 ± 0.01 Cr for alloy (A) and 2.09 ± 0.04 Al and -1.46 ± 0.02 Cr, for alloy (B). Fig. 10 shows the temporal evolution of the Al and Cr γ-matrix supersaturation values for both alloys. The formation of γ'-nuclei during the early stages of aging results in a decrease in the magnitude of the values of $\Delta C_i^{\gamma}(t)$, which in turn causes the slowing and eventual termination of γ'-precipitate nucleation. Beyond the aging time corresponding to the peak γ'-precipitate number density, 1 h for alloy (A) and 4 h for alloy (B),

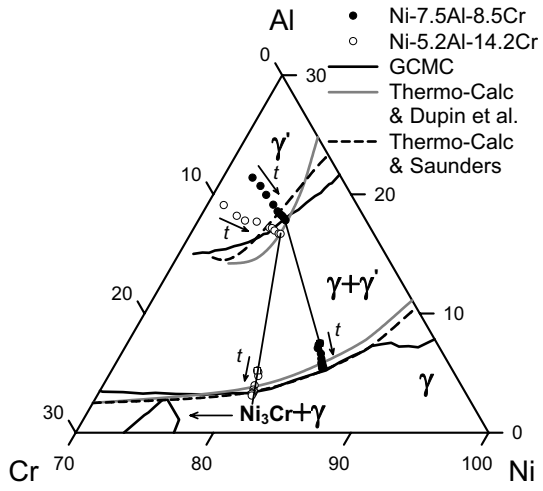

Fig. 8. The compositional trajectories of the γ-matrix and γ'-precipitate phases of alloys (A), Ni–7.5Al–8.5Cr, and (B), Ni–5.2Al–14.2Cr, as they evolve temporally, displayed on a partial Ni–Al–Cr ternary phase diagram at 873 K. The tie-lines are drawn through the nominal compositions of the alloys (squares) and between the experimentally determined equilibrium phase compositions. The trajectories of the γ-matrix phases in alloys (A) and (B) lie approximately on the experimental tie-lines. The trajectories of the γ'-precipitate phases do *not* lie along the tie-line, as predicted by the KV model of isothermal coarsening in ternary alloys [61].

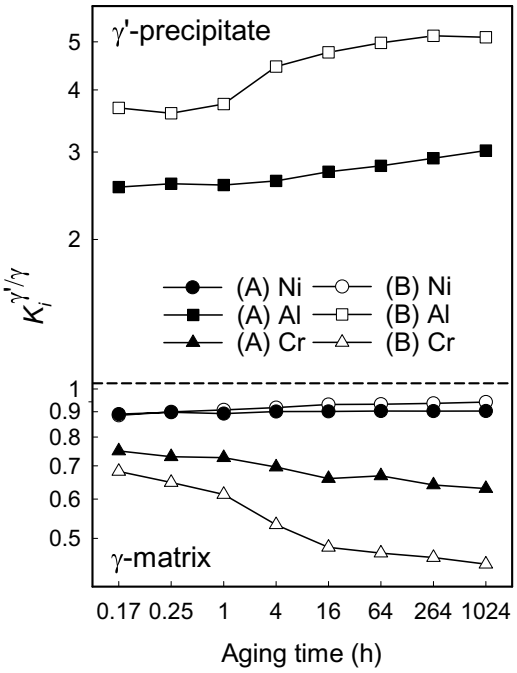

Fig. 9. The partitioning ratios, $K_i^{\gamma'/\gamma}$, of Al and Cr demonstrate that both alloys exhibit partitioning of Al to the γ'-precipitates and Cr to the γ-matrix. Partitioning is more pronounced in alloy (B), where the smaller Al and larger Cr concentration results in a smaller value of the γ-matrix Al solubility and a larger γ-matrix Cr solubility.

the diminution of the $\Delta C_i^{\gamma}(t)$ values approximately follow the $t^{-1/3}$ prediction of the KV model. From Fig. 10, alloy (A) demonstrates a temporal dependence of $t^{-0.32\pm0.03}$ for $\Delta C_{\mathrm{Al}}^{\gamma}(t)$ and $t^{-0.29\pm0.04}$ for $\Delta C_{\mathrm{Cr}}^{\gamma}(t)$, and alloy (B) exhibits a dependence of $t^{-0.33\pm0.04}$ for $\Delta C_{\mathrm{Al}}^{\gamma}(t)$ and $t^{-0.34\pm0.07}$ for $\Delta C_{\mathrm{Cr}}^{\gamma}(t)$. The supersaturation values of the γ'-precipitate

Table 2
Equilibrium γ'-precipitate and γ-matrix equilibrium concentrations, as determined by APT, GCMC simulation and thermodynamic modeling employing Thermo-Calc for alloy (A), Ni–7.5Al–8.5Cr, aged at 873 K

	Ni (at.%)	Al (at.%)	Cr (at.%)
Equilibrium composition of γ'-precipitates			
Measured by APT at 1024 h	76.11 ± 0.09	18.02 ± 0.09	5.87 ± 0.05
Extrapolated from APT data	76.33 ± 0.12	17.82 ± 0.15	5.85 ± 0.12
Modeled by GCMC simulation [44]	76.3 ± 0.5	17.8 ± 0.5	5.9 ± 0.5
Calculated with Thermo-Calc and Saunders database [73]	76.40	17.79	5.81
Calculated with Thermo-Calc and Dupin et al. database [74]	75.44	17.87	6.99
Equilibrium composition of γ-matrix			
Measured by APT at 1024 h	85.13 ± 0.06	5.53 ± 0.07	9.34 ± 0.04
Extrapolated from APT data	85.19 ± 0.08	5.42 ± 0.09	9.39 ± 0.09
Modeled by GCMC simulation [44]	85.8 ± 0.5	5.2 ± 0.5	9.0 ± 0.5
Calculated with Thermo-Calc and Saunders database [73]	85.71	5.42	8.86
Calculated with Thermo-Calc and Dupin et al. database [74]	85.3	5.99	8.70

Table 3
Equilibrium γ'-precipitate volume fraction, ϕ^{eq}, as determined by APT, GCMC simulation and thermodynamic modeling in Thermo-Calc for alloy (A), Ni–7.5Al–8.5Cr, and alloy (B), Ni–5.2Al–14.2Cr, aged at 873 K

Technique used to estimate ϕ^{eq}	(A) Ni–7.5Al–8.5Cr	(B) Ni–5.2Al–14.2Cr
Determined by lever rule calculation with phase compositions measured by APT	16.4 ± 0.6	15.7 ± 0.7
Measured by APT at 1024 h	16.0 ± 5.7	15.6 ± 6.4
Modeled by GCMC simulation [44]	17.5 ± 0.5	15.1 ± 0.5
Calculated with Thermo-Calc and Saunders database [73]	16.69	12.83
Calculated with Thermo-Calc and Dupin et al. database [74]	14.90	12.34

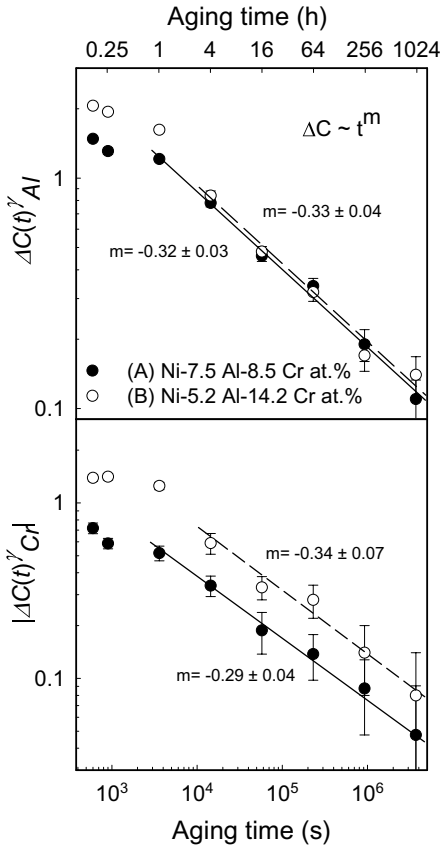

Fig. 10. The magnitude of the values of the supersaturations, $\Delta C_i^{\gamma}(t)$, of Al and Cr in the γ-matrix are smaller for alloy (A), Ni–7.5Al–8.5Cr, than for alloy (B), Ni–5.2Al–14.2Cr. The magnitude of the $\Delta C_i^{\gamma}(t)$ values decrease as $t^{-1/3}$ in the coarsening regimes for both alloys, as predicted by the UO and KV models for isothermal quasi-stationary state coarsening in ternary alloys. The values of $\Delta C_{\mathrm{Cr}}^{\gamma}(t)$ are expressed as an absolute value because they are negative, and reflect a flux of Cr into the γ-matrix with increasing aging time.

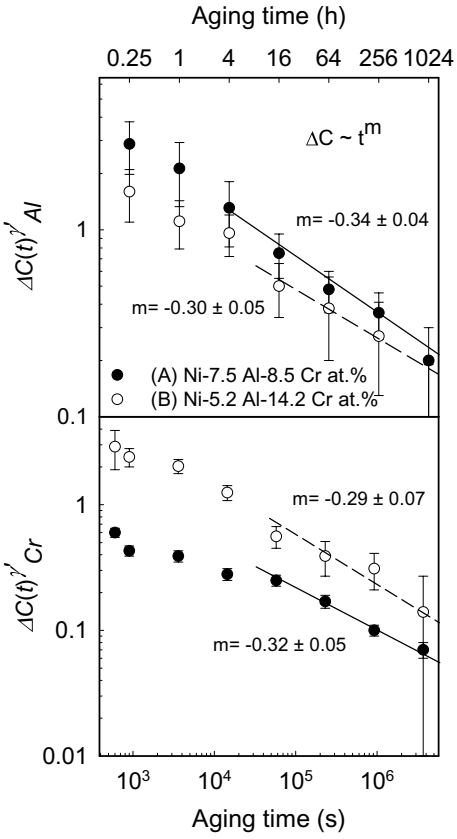

Fig. 11. The supersaturation values of the γ'-precipitates, $\Delta C_i^{\gamma'}(t)$, reflect the chemical compositions of the two alloys, as the value of $\Delta C_{\mathrm{Al}}^{\gamma'}(t)$ is larger in alloy (A), Ni–7.5Al–8.5Cr, which contains more Al, than in alloy (B), Ni–5.2Al–14.2Cr, while the inverse is true for Cr. The values of $\Delta C_i^{\gamma'}(t)$ decrease as approximately $t^{-1/3}$ in the coarsening regimes for both alloys.

phases, $\Delta C_i^{\gamma'}(t)$, of alloys (A) and (B) are a reflection of their alloy composition, as the magnitude of $\Delta C_i^{\gamma'}(t)$ is greater in alloy (A), Ni–7.5Al–8.5Cr, which contains more Al, than in alloy (B), Ni–5.2Al–14.2Cr, while the inverse is true for Cr. From Fig. 11, the quantities $\Delta C_{\mathrm{Al}}^{\gamma'}(t)$ and $\Delta C_{\mathrm{Cr}}^{\gamma'}(t)$ for alloy (A) exhibit temporal dependencies of $t^{-0.34\pm0.04}$ and $t^{-0.32\pm0.05}$, respectively, which are close to the predicted value of $t^{-1/3}$. A dependence of $t^{-0.30\pm0.05}$ for $\Delta C_{\mathrm{Al}}^{\gamma'}(t)$ and of $t^{-0.29\pm0.07}$ for $\Delta C_{\mathrm{Cr}}^{\gamma'}(t)$ are demonstrated for alloy (B).

4. Discussion

While the temporal evolution of the morphology and the volume fraction of the γ'-precipitates in alloy (A), Ni–7.5Al–8.5Cr, and alloy (B), Ni–5.2Al–14.2Cr, are similar, the nanostructural and compositional results for the two alloys exhibit significant differences. These differences can be attributed to the effects of solute concentrations on the kinetic pathways involved in phase decomposition.

4.1. Effects of solute concentration on nucleation behavior

The nucleation behavior observed by APT for alloys (A) and (B) can be compared with the predictions of CNT using Eqs. (2)–(4), given the values of $\sigma^{\gamma/\gamma'}$, ΔF_{ch} and ΔF_{el} for both alloys. The values of $\sigma^{\gamma/\gamma'}$ are estimated as first shown by Ardell for a binary alloy [80,81] and later for a ternary alloy by Marquis and Seidman [82], and as applied to alloy (B) by Sudbrack et al. [40]. The relationship for $\sigma^{\gamma/\gamma'}$ in a nonideal, nondilute ternary alloy consisting of a γ-matrix and a γ'-precipitate phase with a finite volume fraction of the γ'-phase is given by [57]

$$\sigma^{\gamma/\gamma'} = \frac{(K_{\mathrm{KV}})^{1/3}\kappa_{i\mathrm{KV}}^{\gamma}}{2V_{\mathrm{m}}^{\gamma'}p_i}\left(p_{\mathrm{Al}}^2 G_{\mathrm{Al,Al}}^{\gamma} + p_{\mathrm{Al}}p_{\mathrm{Cr}}G_{\mathrm{Al,Cr}}^{\gamma} + p_{\mathrm{Cr}}^2 G_{\mathrm{Cr,Cr}}^{\gamma}\right), \tag{9}$$

where K_{KV} and $\kappa_{i,\mathrm{KV}}^{\gamma}$ are the rate constants for the quantities $\langle R(t)\rangle$ and $\Delta C_i^{\gamma}(t)$, respectively, from the KV coarsening model, p_i is the magnitude of the partitioning as previously defined, $V_{\mathrm{m}}^{\gamma'}$ is the molar volume of the γ'-precipitate phase, calculated to be $6.7584 \times 10^{-6}\ \mathrm{m^3\ mol^{-1}}$, and $G_{i,j}^{\gamma}$ is shorthand notation for the partial derivatives of the molar Gibbs free energy of the γ-matrix phase with re-

spect to the solute species i and j. The quantities K_{KV} and $\kappa^{\gamma}_{i,KV}$ are determined by fitting the experimental APT data to Eqs. (5) and (7) from the KV coarsening model. For alloy (A), K_{KV} is $(1.84 \pm 0.43) \times 10^{-31}$ m^3 s^{-1} and $\kappa^{\gamma}_{Al,KV}$ and $\kappa^{\gamma}_{Cr,KV}$ are 0.18 ± 0.05 and -0.06 ± 0.01 at. fr. s$^{1/3}$, respectively, while a value of K_{KV} of $(8.8 \pm 3.3) \times 10^{-32}$ m^3 s^{-1} and values of $\kappa^{\gamma}_{Al,KV}$ and $\kappa^{\gamma}_{Cr,KV}$ of 0.19 ± 0.02 and -0.14 ± 0.05 at. fr. s$^{1/3}$ are found for alloy (B). For the general case described by nonideal and nondilute solution theory, the values of $G^{\gamma}_{i,j}$ may be calculated using Thermo-Calc employing the extant databases for nickel-based superalloys. As noted by Sudbrack et al. [40], the calculations of $G^{\gamma}_{i,j}$ from Thermo-Calc predict a more highly curved free energy surface than ideal solution theory with respect to all solute species combinations. The Thermo-Calc assessments take into account the excess free energies of mixing and the magnitudes of $G^{\gamma}_{i,j}$ are 1.5–13 times larger than those for ideal solution theory for alloys (A) and(B), as shown in Table 4 for alloy (A). See Table 4 in Sudbrack et al. [40] for the values of $G^{\gamma}_{i,j}$ for alloy (B).

Fortuitously, the Thermo-Calc and ideal solution theory assessments of $G^{\gamma}_{i,j}$ yield approximately the same value for $\sigma^{\gamma/\gamma'}$ for alloy (B) of 22–23 $\pm$ 7 mJ m^{-2} [40]. For alloy (A), the values for $\sigma^{\gamma/\gamma'}$ calculated from the ideal solution theory of 14–16 $\pm$ 3 mJ m^{-2} are smaller than those from the Thermo-Calc assessment of $G^{\gamma}_{i,j}$ of 23–25 $\pm$ 6 mJ m^{-2} (Table 5). For the purposes of CNT, values of $\sigma^{\gamma/\gamma'}$ of 24 ± 6 mJ m^{-2} for alloy (A) and 22.5 ± 7 mJ m^{-2} for alloy (B) are used, the averages of the values generated from the Thermo-Calc assessments of $G^{\gamma}_{i,j}$. Additionally, estimates of 36.3 ± 3.8 and 35.7 ± 1.7 mJ m^{-2} are obtained for alloys (A) and (B) at 0 K from first-principles calculations, in the framework of density functional theory and the local density approximation, employing ultrasoft Vanderbilt potentials, using the Vienna Ab Initio Simulation Package code [83–86]. It is noted that the values of $\sigma^{\gamma/\gamma'}$ from the first-principles calculations are larger than those determined experimentally because the first-principles calculations assume a sharp γ/γ' interface and are performed at 0 K, and therefore do not include entropic effects. The experimental estimates of $\sigma^{\gamma/\gamma'}$ are for experimentally diffuse γ/γ' interfaces at 873 K and are free energies because they include entropic effects.

A value of $\sigma^{\gamma/\gamma'}$ of 12.5 mJ m^{-2} was previously determined for a ternary Ni–5.2Al–14.8Cr alloy aged at 873 K by Schmuck et al. [22]. The value of $\sigma^{\gamma/\gamma'}$ for this alloy, which has an overall composition that is very close to that of alloy (B) (Ni–5.2Al–14.2Cr), was determined assuming the LSW model for binary alloys. We reanalyzed their data according to the method developed by Marquis and Seidman for ternary alloys and estimated values of 20–21 ± 5 mJ m^{-2} for $\sigma^{\gamma/\gamma'}$, in good agreement with the values of $\sigma^{\gamma/\gamma'}$ estimated for alloys (A) and (B); additional details are presented in Appendix. Gleiter and Hornbogen [87] estimated a value of 13.5 mJ m^{-2} for an Ni–5.4Al–18.7Cr alloy aged at 750 °C, though they also applied binary LSW theory to a ternary alloy and their results did not include concentration data, making recalculation of their value of $\sigma^{\gamma/\gamma}$ impossible by the method developed by Marquis and Seidman for ternary alloys. Baldan [3] provides a review of literature values of $\sigma^{\gamma/\gamma'}$ for several different Ni–Al and Ni–Al–Cr systems over a range of aging temperatures, which need to be evaluated in detail in light of our work.

The values of the chemical driving force of alloys (A) and (B) are estimated as proposed by Lupis [88] and applied by Schmuck et al. [22] from thermodynamic data taken from Thermo-Calc [72] and the extant nickel-based superalloy databases [73,74]. The values of ΔF_{ch} for alloys (A) and (B) are estimated to be -6.6×10^7 and -8.2×10^7 J m^{-3}, respectively. The values of ΔF_{el} for the two alloys are estimated using [89]:

$$\Delta F_{el} = \frac{2S^{\gamma}B^{\gamma'}(V_a^{\gamma'} - V_a^{\gamma})^2}{(3B^{\gamma'} + 4S^{\gamma})V_a^{\gamma'}}, \tag{10}$$

where S^{γ} is the shear modulus of the γ-matrix phase, $B^{\gamma'}$ is the bulk modulus of the γ'-precipitate phase, and V_a^{γ} and $V_a^{\gamma'}$ are the atomic volumes of the γ-matrix and

Table 4
Curvatures in the molar Gibbs free energy surface of the γ-matrix phase evaluated at the equilibrium composition with respect to components i and j, $G^{\gamma}_{i,j}$, obtained from ideal solution theory and Thermo-Calc thermodynamic assessments for alloy (A), Ni–7.5Al–8.5Cr, aged at 873 K

$G^{\gamma}_{i,j}$	Ideal solution theory (J mol^{-1})	Saunders database [73] (J mol^{-1})	Dupin et al. database [74] (J mol^{-1})
$G^{\gamma}_{Al,Al}$	142,441.7	271,392.5	306,697.8
$G^{\gamma}_{Cr,Cr}$	85,821.1	166,601.4	166,708.5
$G^{\gamma}_{Al,Cr}$	8521.4	112,567.3	140,244.9

Table 5
Free energy of the γ/γ' interfaces, $\sigma^{\gamma/\gamma'}$, at 873 K in Ni–7.5Al–8.5Cr calculated from the experimental values of the Kuehmann–Voorhees coarsening rate constants for the average precipitate radius and the supersaturation of solute species i employing Eq. (9) with solution thermodynamics described by the ideal solution and Thermo-Calc databases given in Table 4

Thermodynamic models	$\sigma^{\gamma/\gamma'}_{Al}$ (mJ m^{-2})	$\sigma^{\gamma/\gamma'}_{Cr}$ (mJ m^{-2})	$\sigma^{\gamma/\gamma'}$ (mJ m^{-2})
Ideal solution theory	14.2 ± 3.1	16.0 ± 3.6	15.1 ± 3.4
Saunders database [73]	21.6 ± 4.0	24.4 ± 6.1	23.0 ± 5.1
Dupin et al. database [74]	23.6 ± 4.9	26.6 ± 6.2	25.1 ± 5.5

γ'-precipitate phases, respectively. No elastic constants are available for this alloy, therefore the value of S^{γ} of 100.9 GPa, of a similar alloy, Ni–12.69Al at 873 K [90] is employed, while the value of $B^{\gamma'}$ is taken to be 175 GPa [91]. The lattice parameters for the equilibrium phases in alloy (A) at 873 K are estimated to be 0.3554 ± 0.0001 and 0.3544 ± 0.0001 nm for the γ' and γ-phases, respectively, based on room-temperature X-ray diffraction measurements on similar Ni–Al–Cr alloys [6,11]. These lattice parameter values result in a near-zero estimate of the lattice misfit of 0.0027 ± 0.0004 for alloy (A). The lattice parameter misfit for alloy (B) is estimated to be 0.0006 ± 0.0004 [37]. Substituting these values into Eq. (10) yields values of ΔF_{el} of 2.5×10^6 J m^{-3} for alloy (A) and 1.1×10^5 J m^{-3} for alloy (B). The larger Cr concentration in alloy (B) is responsible for a smaller value of the lattice parameter misfit and therefore a smaller elastic strain energy. The quantity ΔF_{el} is also estimated by a simpler technique due to Eshelby [92], which yields values of 2.80×10^6 and 1.38×10^5 J m^{-3} for alloys (A) and (B), respectively. The high degree of coherency of the γ'-precipitates in these alloys is such that the bulk component of the driving force for nucleation is dominated by the ΔF_{ch} term, as ΔF_{el} is only 3.9% of the value of ΔF_{ch} for alloy (A) and 0.1% for alloy (B). As such, experimentally determined differences in the nucleation behavior may be described as due primarily, but not exclusively, to differing values of ΔF_{ch}. The tracer diffusivity of Al in the γ-matrix phase of these Ni–Al–Cr alloys is significantly larger than the diffusivity of Cr. For alloy (A), D_{Al}^{fcc} is 11×10^{-21} m^{2}s^{-1} and D_{Cr}^{fcc} is 3.0×10^{-21} m^2 s^{-1}, while for alloy (B), D_{Al}^{fcc} is 9.6×10^{-21} m^2 s^{-1} and D_{Cr}^{fcc} has a value of 2.6×10^{-21} m^2 s^{-1}. As such, the kinetics of the early stages of the phase transformation of alloy (A), Ni–7.5Al–8.5Cr, are expected to be faster than those involved in the decomposition of alloy (B), Ni–5.2Al–14.2Cr, as a result of the larger Al concentration of alloy (A) and the larger Cr concentration of alloy (B).

The value of W_R^* for alloy (A) is estimated from Eq. (2) to be 35.2 kJ mol^{-1} or 0.365 eV atom^{-1}, while R^* is estimated from Eq. (3) to be 0.76 nm. The value of W_R^* for alloy (B) is found to be 17.0 kJ mol^{-1} or 0.177 eV atom^{-1}, and R^* is calculated to be 0.55 nm. The nucleation currents for the two alloys are estimated from Eq. (4) to be 4.0×10^{22} m^{-3} s^{-1} for alloy (A) and 3.2×10^{23} m^{-3} s^{-1} for alloy (B). The calculated values of $\sigma^{\gamma/\gamma'}$, ΔF_{ch}, ΔF_{el}, W_R^*, R^*, and J^{st} for both alloys are summarized in Table 6.

The predictions of the value of R^* from CNT are verified experimentally for both alloys, as the first nucleating precipitates detected consistently by APT at an aging time of 1/6 h have $\langle R(t) \rangle$ values of 0.90 ± 0.32 nm for alloy (A) and 0.74 ± 0.24 nm for alloy (B), which are both slightly greater than the calculated R^* estimates of 0.76 and 0.55 nm, respectively. The predicted value of J^{st} of 4.0×10^{22} m^{-3} s^{-1} for alloy (A) is nearly an order of magnitude greater than the experimental value of $(5.4 \pm 1.5) \times 10^{21}$ m^{-3} s^{-1}. The calculated value of J^{st} for alloy (B) of 3.2×10^{23} m^{-3} s^{-1} is 50 times greater than the experimentally measured value of J^{st} of $(5.9 \pm 1.7) \times 10^{21}$ m^{-3} s^{-1}. Given the evidence of precursor clustering in these Ni–Al–Cr alloys [36], it is surprising that the experimentally determined values of J^{st} are significantly less than the predicted values. Xiao and Haasen [10] performed a similar comparison of experimentally determined nucleation currents with those predicted by CNT for a binary Ni–12.0Al at.% alloy aged at 773 K and found that the predicted value of J^{st} was a factor of 500 larger than the measured value of J^{st}. They attributed this discrepancy to the sensitivity of the predicted value of J^{st} to the value of R^*. Xiao and Haasen also pointed out that predicted nucleation currents are likely to be overestimates due to the assumption that the value of N_0 is equal to the volume density of lattice sites, which is a commonly made assumption that is not necessarily correct. By assuming that the value of N_0 is equal to the volume density of Al atoms, we seem to have mitigated this error to some extent. Given that the experimentally determined values of J^{st} are measured from two experimental data points, and that the detailed kinetics involved in the formation of γ'-nuclei in these ternary systems are not completely understood, further analysis is presently not instructive. The nucleation behavior of Ni–Al–Cr alloys certainly warrants future research, given the technological importance of these systems.

The formation of stable, growing nuclei at early aging times causes a decrease in the values of $\Delta C_i^{\gamma}(t)$ and results in a reduction in, and the eventual termination of, nucleation. By an aging time of 1 h, the values of $\Delta C_i^{\gamma}(t)$ for alloy (A) decrease from the solid-solution values of 2.08 ± 0.02 Al and -0.89 ± 0.01 Cr to 1.21 ± 0.02 Al and -0.52 ± 0.04 Cr. This decrease in the magnitude of the $\Delta C_i^{\gamma}(t)$ values is reflected in a 50% decrease in the quantity ΔF_{ch} to a value of -3.3×10^7 J m^{-3}, and therefore a decrease in the predicted value of J^{st} of seven orders of magnitude, after only 1 h of aging. After 4 h of aging in alloy (B), the values of $\Delta C_i^{\gamma}(t)$ decrease from 2.09 ± 0.04 Al and -1.46 ± 0.02 Cr, to 0.84 ± 0.04 Al and -0.59 ± 0.09 Cr, while the value of ΔF_{ch} decreases 51% to -4.01×10^7 J m^{-3}. This decrease in the quantity ΔF_{ch}

Table 6
The interfacial free energy, $\sigma^{\gamma/\gamma'}$, the chemical free energy, ΔF_{ch}, and the elastic strain energy, ΔF_{el}, components of the driving force for nucleation used to estimate the net reversible work, W_R^*, required for the formation of critical nuclei of size, R^*, and the nucleation current, J^{st}, according to classical nucleation theory

Alloy	$\sigma^{\gamma/\gamma'}$ (mJ m^{-2})	ΔF_{ch} ($\times 10^7$ J m^{-3})	ΔF_{el} ($\times 10^6$ J m^{-3})	W_R^* (kJ mol^{-1})	R^* (nm)	J^{st} (m^{-3} s^{-1})
(A) Ni–7.5Al–8.5Cr	24.0 ± 6	-6.6	2.5	35.2	0.76	4.0×10^{22}
(B) Ni–5.2Al–14.2Cr	22.5 ± 7	-8.2	0.11	17.0	0.55	3.2×10^{23}

results in a decrease in the predicted value of J^{st} of three orders of magnitude for alloy (B). From these estimates, and our APT nanostructural results, it appears that the larger initial value of the chemical driving force in alloy (B) sustains a significant nucleation current for aging times as long as 4 h, whereas the nucleation current decreases significantly in alloy (A) after 1 h.

4.2. Effects of solute concentration on the coarsening behavior

As alloys (A) and (B) coarsen, the quantities $\Delta C_i^{\gamma}(t)$ and $\Delta C_i^{\gamma'}(t)$ evolve temporally as approximately $t^{-1/3}$ and $\langle R(t)\rangle$ grows as approximately $t^{1/3}$, as predicted by the UO and KV models. The experimentally measured temporal dependencies of $N_v(t)$ of $t^{-0.42\pm0.03.}$ and $t^{-0.67\pm0.01}$ for alloys (A) and (B), respectively, differ significantly, however, from the t^{-1} prediction of both models. The magnitudes of the quantities $\Delta C_i^{\gamma}(t)$ for both alloys remain nonzero at an aging time of 1024 h, thus neither alloy has achieved a true stationary state, which is a basic assumption of classical LSW Ostwald ripening behavior. The UO and KV models, however, assume a quasi-stationary state, which may have been achieved for alloys (A) and (B). At 1024 h, the value of ϕ, Fig. 6, is still evolving temporally.

When Ostwald ripening is considered to be a diffusion-limited process, it is limited by the characteristic length over which diffusion can occur, taken as the average edge-to-edge interprecipitate spacing in these systems. It is important to note that as $N_v(t)$ decreases with increasing time, $\langle R(t)\rangle$ increases and the value of $\langle\lambda_{e\text{–}e}\rangle$ increases concomitantly. The time required to reach stationary-state coarsening, t_c, may be estimated employing [93]:

$$t_c \approx \frac{64}{729}\left(\frac{\omega_3}{\omega_2}\right)^6\left(\frac{1}{\phi}-1\right)^6\frac{K_{KV}^2}{D^3}, \tag{11}$$

where K_{KV} is the coarsening rate constant for $\langle R(t)\rangle$ as defined in Section 1.2, ω_i is the ith moment of the precipitate size distribution, $\omega_2 = 1.046$ and $\omega_3 = 1.130$ for the LSW distribution [94], and D is the diffusivity of the least mobile atomic species in the alloy, taken to be the diffusivity of Cr in the γ'-precipitate phase, which has a value of $1.44\times10^{-23}\ m^2\ s^{-1}$ at 873 K [95]. The estimate of t_c for alloy (A) from Eq. (11) is $(8\pm5)\times10^6$ h, while the predicted value of t_c for alloy (B) is $(2\pm1)\times10^6$ h, both of which are greater than the longest aging time studied, 1024 h. Our inability to achieve stationary-state coarsening explains the continuously increasing values of ϕ and the nonzero values of $\Delta C_i^{\gamma}(t)$ and $\Delta C_i^{\gamma'}(t)$ at an aging time of 1024 h, which may explain the deviation from the t^{-1} prediction for the temporal evolution of $N_v(t)$. When D is taken to be the diffusivity of Cr in the γ-matrix phase, $3.0\times10^{-21}\ m^2\ s^{-1}$ for alloy (A) and $2.6\times10^{-21}\ m^2\ s^{-1}$ for alloy (B), the estimates of t_c of (1.0 ± 0.1) and (0.3 ± 0.1) h generated for alloy (A) and (B), respectively, are three orders of magnitude less then the longest aging time studied experimentally and indicate that the diffusivity inside the γ'-precipitates may be the rate limiting step in γ'-precipitate coarsening. Additionally, the values of t_c for alloy (A) are longer than those estimated for alloy (B), an indication that the coarsening kinetics are slower in alloy (A). Thus the rate of the diminution of $N_v(t)$ is significantly slower in alloy (A) ($N_v(t) \propto t^{-0.42\pm0.03}$) than in alloy (B) ($N_v(t) \propto t^{-0.67\pm0.01}$).

A recent study by Mao et al. [32] combined APT and LKMC to study the role of the precipitation diffusion mechanism on the early-stage precipitate morphology of alloy (B). They showed that the long range vacancy–solute binding energies (out to the fourth-nearest-neighbor distance) strongly affect the γ'-precipitate coagulation and coalescence process, which occurs abundantly at early stages, from 1/4 to 64 h. Coagulation and coalescence are shown to result from the overlap of nonequilibrium concentration profiles surrounding γ'-precipitates that give rise to nonequilibrium diffuse interfaces. The concentration profiles associated with the interfacial regions between γ'-precipitates are spread over distances significantly larger than that of the equilibrium interfacial thickness. This is due to specific couplings between the diffusion fluxes of the constituent elements toward and away from γ'-precipitates, which are a result of the finite vacancy–solute binding energies. From this analysis, the coagulation and coalescence of γ'-precipitates is more likely when $\langle\lambda_{e\text{–}e}\rangle$ has a minimum value, as evidenced experimentally for alloys (A) and (B), Fig. 5. Additionally, the larger Al concentration in alloy (A) leads to the formation of more highly mobile Al clusters than in alloy (B), which explains why the quantities $N_v(t)$ and f achieve their maximum values, and the quantity $\langle\lambda_{e\text{–}e}\rangle$ reaches a minimum value, after aging for only 1 h in alloy (A), while this condition is reached at 4 h in alloy (B).

5. Summary and conclusions

We present a detailed comparison of the nanostructural and compositional evolution of alloy (A), Ni–7.5Al–8.5Cr, and alloy (B), Ni–5.2Al–14.2Cr, during phase separation at 873 K for aging times ranging from 1/6 to 1024 h, employing APT. These ternary alloys have similar equilibrium γ'-precipitate volume fractions, ϕ^{eq}, of $16.4\pm0.6\%$ for alloy (A) and $15.7\pm0.7\%$ for alloy (B), and were designed to study the effects of solute concentration on the kinetic pathways in model Ni–Al–Cr alloys, leading to the following results:

- The morphology of the γ'-precipitate phase in both alloys is found by both APT and TEM to be spheroidal for aging times as long as 1024 h, as a result of a near-zero lattice parameter misfit between the γ-matrix and γ'-precipitate phases. This high degree of coherency makes these alloys amenable to a comparison of APT results to predictions of classical theories of nucleation, growth and coarsening where the chemical free energy

term is dominant. Coagulation and coalescence of γ'-precipitates is observed and is argued to be a result of the overlap of the nonequilibrium concentration profiles associated with adjacent γ'-precipitates [32].

- After aging to 1/6 h, precipitation of the γ'-phase is evident for both alloys, as alloy (A) forms nuclei with a composition of 70.9 ± 1.4 Ni, 23.3 ± 1.5 Al and 5.8 ± 0.9 Cr at a γ'-precipitate number density, $N_v(t = 1/6\text{h})$, of $(2.6 \pm 1.4) \times 10^{23}$ m^{-3}, a mean radius, $\langle R(t = 1/6\text{h})\rangle$, of 0.90 ± 0.32 nm and a volume fraction, ϕ, of $0.31 \pm 0.11\%$. Alloy (B) forms 71.3 ± 1.6 Ni, 19.1 ± 1.4 Al and 9.7 ± 1.1 Cr nuclei with a $N_v(t = 1/6$ h) value of $(3.6 \pm 1.3) \times 10^{23}$ m^{-3}, an $\langle R(t = 1/6\text{h})\rangle$ value of 0.74 ± 0.24 nm and a ϕ value of $0.11 \pm 0.04\%$.
- CNT is applied to demonstrate that the chemical free energy changes for forming a nucleus, ΔF_{ch}, of -6.6×10^7 J m^{-3} for alloy (A) and -8.2×10^7 J m^{-3} for alloy (B), provide the primary driving force for nucleation. As such, the differing solute concentrations of the two alloys are responsible for differences in the nucleation behavior and in the nanostructural and compositional evolution of the alloys as they decompose. The high degree of γ'-precipitate coherency with the γ-matrix in these alloys is such that the elastic strain energy values, ΔF_{el}, estimated to be -2.5×10^6 J m^{-3} for alloy (A) and -1.1×10^5 J m^{-3} for alloy (B), are only a small fraction of the values of ΔF_{ch}, for both alloys.
- Estimates of the γ/γ' interfacial free energy values, $\sigma^{\gamma/\gamma'}$, from the coarsening data obtained by APT yield values of $23–25 \pm 6$ mJ m^{-2} for alloy (A) and $22–23 \pm 7$ mJ m^{-2} for alloy (B). These values are in good agreement with our recalculated values of $\sigma^{\gamma/\gamma'}$ of $20–21 \pm 5$ mJ m^{-2} for the coarsening data of Schmuck et al. [22] for a ternary Ni–5.2Al–14.8Cr alloy aged at 873 K.
- The predictions of the critical radii for nucleation, R^*, of 0.76 and 0.55 nm for alloys (A) and (B) show reasonable agreement with the average radii of the first γ'-precipitates detected by APT at 1/6 h, of 0.90 ± 0.32 and 0.74 ± 0.24 nm, respectively. The predicted value of J^{st} of 4.0×10^{22} m^{-3} s^{-1} for alloy (A) is nearly one order of magnitude greater than the experimental value of $(5.4 \pm 1.5) \times 10^{21}$ m^{-3} s^{-1}, and the calculated value of J^{st} for alloy (B) of 3.2×10^{23} m^{-3} s^{-1} is 50 times greater than the experimentally measured value of J^{st} of $(5.9 \pm 1.7) \times 10^{21}$ m^{-3} s^{-1}. This discrepancy may be due to the sensitivity of the predicted value of J^{st} to the value of R^* and to the assumption that the number of nucleation sites per volume is equal to the volume density of lattice points occupied by Al, the precipitate-forming solute element, which may be an overestimate. Further research is required to measure the value of J^{st} more accurately for ternary Ni–Al–Cr alloys to better understand the nucleation kinetics in these concentrated multicomponent alloys. To date, there is no generally accepted theory of nucleation in concentrated multicomponent alloys.
- After 1 h of aging, alloy (A) achieves a peak value of $N_v(t)$ of $(2.21 \pm 0.64) \times 10^{24}$ m^{-3}, which coincides with a minimum value of the average interprecipitate edge-to-edge spacing, $\langle \lambda_{e-e}\rangle$, of 7.0 ± 2.5 nm and a maximum in the fraction of interconnected precipitates, f, of $18 \pm 4\%$. At an aging time of 4 h, alloy (B) achieves a peak value of $N_v(t)$ of $(3.2 \pm 0.6) \times 10^{24}$ m^{-3} at a minimum value of $\langle \lambda_{e-e}\rangle$ of 5.9 ± 0.8 nm and a maximum value of f of $30 \pm 4\%$. The larger peak value of $N_v(t)$ for alloy (B) is a result of the larger initial solid-solution value of ΔF_{ch} in alloy (B), which sustains nucleation for longer aging times.
- In the growth and coarsening regime that follows the peak in the value of $N_v(t)$, the quantity $\langle R(t)\rangle$ displays a temporal dependence of $t^{0.29\pm0.03}$ for alloy (A) and $t^{0.29\pm0.05}$ for alloy (B), in approximate agreement with the $t^{1/3}$ prediction of the KV model for isothermal coarsening in concentrated ternary alloys. The supersaturation of the γ-matrix phase in alloy (A) exhibits a temporal dependence of $t^{-0.32\pm0.03}$ for Al and $t^{-0.29\pm0.04}$ for Cr, while alloy (B) demonstrates a temporal dependence of $t^{-0.33\pm0.04}$ for Al and $t^{-0.34\pm0.07}$ for Cr, in good agreement with the $t^{-1/3}$ prediction of the UO and KV models. The supersaturation values of Al and Cr in the γ'-precipitate phase of Alloy (A) display a temporal dependence of $t^{-0.34\pm0.04}$ for Al and $t^{-0.32\pm0.05}$ for Cr, while the supersaturation values in alloy (B) demonstrate a temporal dependence of $t^{-0.30\pm0.05}$ for Al and $t^{-0.29\pm0.07}$ for Cr.
- During growth and coarsening, the diminution of the quantity $N_v(t)$ in alloy (A) exhibits a temporal dependence of $t^{-0.42\pm0.03}$, while alloy (B) exhibits a temporal dependence of $t^{-0.67\pm0.01}$. These temporal exponents deviate from the t^{-1} prediction of the KV coarsening model because neither alloy has achieved stationary-state coarsening, characterized by a constant value of ϕ and a zero value of the γ-matrix supersaturation. The estimate of the critical time required for stationary-state coarsening, t_c, for alloy (A) is $(8 \pm 5) \times 10^6$ h, while the value for alloy (B) is $(2 \pm 1) \times 10^6$ h. The estimates of t_c for both alloys are far beyond the longest aging time we studied, 1024 h, and this is most likely the reason that stationary-state coarsening is not achieved.
- The compositional trajectories of the γ-matrix during phase decomposition lie approximately along the tie-lines, while the trajectories of the γ'-precipitate phase do not, as predicted by the KV model for quasi-stationary state isothermal coarsening in ternary alloys. The addition of a third alloying element alters the Gibbs–Thompson equations significantly, and as such the KV model predicts that the compositional trajectory of the γ'-precipitate phase will lie on a straight line that is not necessarily parallel to the equilibrium tie-line.
- The solute solubility in the γ-matrix phase of alloy (A) is determined by APT to be 5.42 ± 0.09 Al and 9.39 ± 0.09 Cr, and 3.13 ± 0.08 Al and 15.61 ± 0.18 Cr for alloy (B).

Table 7
Equilibrium γ'-precipitate and γ-matrix equilibrium concentrations, as determined by APT and Thermo-Calc for Ni–5.2Al–14.8Cr aged at 873 K from the data of Schmuck et al. [22]

	Ni (at.%)	Al (at.%)	Cr (at.%)
Equilibrium composition of γ'-precipitates			
Measured by APT at 64 h [22]	74 ± 2	18 ± 1	7.6 ± 0.8
Extrapolated from APT data [22]	74.2 ± 0.9	18.4 ± 0.8	7.4 ± 0.5
Calculated with Thermo-Calc and Saunders database [73]	74.91	16.08	9.01
Calculated with Thermo-Calc and Dupin database [74]	75.79	14.44	9.76
Equilibrium composition of γ-matrix			
Measured by APT at 64 h [22]	80.2 ± 0.3	4 ± 0.2	15.8 ± 0.2
Extrapolated from APT data [22]	80.3 ± 0.2	3.94 ± 0.08	15.8 ± 0.2
Calculated with Thermo-Calc and Saunders database [73]	80.80	3.50	15.70
Calculated with Thermo-Calc and Dupin database [74]	80.65	3.77	15.58

The equilibrium composition of the γ'-precipitates is 76.33 ± 0.12 Ni, 17.82 ± 0.15 Al and 5.85 ± 0.12 Cr for alloy (A) and 76.53 ± 0.25 Ni, 16.69 ± 0.22 Al and 6.77 ± 0.15 Cr for alloy (B). The partitioning ratios of the two alloys differ significantly, Fig. 9, due to the differences in the kinetic pathways that lead to decomposition in the two alloys.

Acknowledgements

This research was sponsored by the National Science Foundation (NSF) under grant DMR-0241928. C.B.M. and C.K.S. received partial support from Le Fonds québécois de la recherche sur la nature et les technologies (FQRNT) and NSF graduate research fellowships, respectively. J.W. was supported by an NSF REU award when she was an undergraduate at Northwestern University. APT measurements were performed at the Northwestern University Center for Atom-probe Tomography (NUCAPT). The LEAP™ tomograph was purchased with funding from the NSF-MRI (DMR 0420532, Dr. Charles Bouldin, grant officer) and ONR-DURIP (N00014-0400798, Dr. Julie Christodoulou, grant officer) programs. Additionally, the LEAP™ tomograph was enhanced in April 2006 with a picosecond laser with funding from the ONR-DURIP (N00014-0610539, Dr. Julie Christodoulou, grant officer). The TEM work was performed in the EPIC facility of the NUANCE Center at Northwestern University. The NUANCE Center is supported by NSF-NSEC, NSF-MRSEC, the Keck Foundation, the State of Illinois, and Northwestern University. We extend our gratitude to Dr. Kevin Yoon for his assistance with Thermo-Calc, to Dr. Carelyn Campbell for diffusivity calculations, and to Dr. Georges Martin for discussions.

Appendix

Schmuck et al. [22] determined a value for the interfacial free energy, $\sigma^{\gamma/\gamma'}$, of 12.5 mJ m^{-2} for a ternary Ni–5.2Al–14.8Cr alloy aged at 873 K. This value is approximately one half the value determined by Sudbrack et al. [40] for a similar alloy Ni–5.2Al–14.2Cr aged at 873 K. The Schmuck et al. approach assumes: (i) the LSW model for binary alloys applies to their ternary system; (ii) the rate constant for the average γ'-precipitate radius from LSW is correct, which it is not [96]; and (iii) that the γ-matrix and γ'-precipitate phase compositions achieved their equilibrium compositions after aging for 64 h. We recalculate the values of $\sigma^{\gamma/\gamma'}$ from the data by Schmuck et al. by applying a relationship for $\sigma^{\gamma/\gamma'}$ in a nonideal, nondilute ternary alloy proposed by Marquis and Seidman [82], based on the results of Calderon et al. [96] and the Kuehmann–Voorhees coarsening model [61], and as applied to alloy (B) by Sudbrack et al. [40]. Schmuck et al. found that the γ'-precipitates had compositions very close to their equilibrium values after only 1 h, and had achieved their equilibrium compositions after 64 h. Sudbrack et al. [40], however, found that the γ'-precipitate phase compositions of a similar alloy, alloy (B) Ni–5.2Al–14.2Cr aged at 873 K, continued to evolve temporally at an aging time of 1024 h. As a result, we use the equilibrium compositions calculated by Thermo-Calc for Ni–5.2Al–14.8Cr, employing the Saunders database [73] (Table 7), in our estimates of the value of $\sigma^{\gamma/\gamma'}$ for the data of Schmuck et al. A coarsening rate constant, K_{KV}, of $(2.30 \pm 0.13) \times 10^{-31}$ m^3 s^{-1} and values of $\kappa^{\gamma}_{Al,KV}$ and $\kappa^{\gamma}_{Cr,KV}$ of 0.13 ± 0.01 and -0.08 ± 0.02 at. fr. s$^{1/3}$, respectively, are found from the data of Schmuck et al. These values should be compared to values of K_{KV} of $(8.8 \pm 3.3) \times 10^{-31}$ m^3 s^{-1} and of 0.19 ± 0.02 and -0.14 ± 0.05 at. fr. s$^{1/3}$, for $\kappa^{\gamma}_{Al,KV}$ and $\kappa^{\gamma}_{Cr,KV}$ respectively, for alloy (B). The value of $\sigma^{\gamma/\gamma'}$ recalculated from the data of Schmuck et al. using Eq. (9) is 20–21 ± 5 mJ m^{-2}, which is in good agreement with values of 22–23 ± 7 mJ m^{-2} for alloy (B) and 23–25 ± 6 mJ m^{-2} for alloy (A).

References

[1] Durand-Charre M. The microstructure of superalloys. Amsterdam: Gordon and Breach Science; 1997.
[2] Argon AS. Strengthening mechanisms in crystal plasticity. Oxford: Oxford University Press; 2007.
[3] Baldan A. J Mater Sci 2002;37:2379–405.
[4] Reed RC. The superalloys: fundamentals and applications. New York: Cambridge University Press; 2006.

[5] Hirata T, Kirkwood DH. Acta Metall 1977;25:1425–34.
[6] Taylor A, Floyd W. J Inst Metals 1952;81:451–64.
[7] Ardell AJ, Nicholson RB. J Phys Chem Solids 1966;27:1793–804.
[8] Kirkwood DH. Acta Metall 1970;18:563–70.
[9] Chellman DJ, Ardell AJ. Acta Metall 1974;22:577–88.
[10] Xiao SQ, Haasen P. Acta Metall Mater 1991;39:651–9.
[11] Hornbogen E, Roth M. Z Metall 1967;58:842–55.
[12] Royer A, Bastie P, Veron M. Acta Mat 1998;46:5357–68.
[13] Broz P, Svoboda M, Bursik J, Kroupa A, Havrankova J. Mater Sci Eng, A 2002;A325:59–65.
[14] Messoloras S, Stewart RJ. J Appl Crystall 1988;21:870–2.
[15] Beddoe R, Haasen P, Kostorz G. Early stages of decomposition in Ni–Al single crystals studied by small-angle neutron scattering. In: Haasen PGV, Wagner R, Ashby MF, editors. Decomposition of alloys: the early stages. Oxford: Pergamon Press; 1984.
[16] Staron P, Kampmann R. Acta Mat 2000;48:701–12.
[17] Gilles R, Mukherji D, Hoelzel M, Strunz P, Toebbens DM, Barbier B. Acta Mat 2006;54:1307–16.
[18] Wendt H, Haasen P. Acta Metall 1983;31:1649–59.
[19] Vanbakel GPEM, Hariharan K, Seidman DN. Appl Surf Sci 1995;90:95–105.
[20] Al–Kassab T, Wollenberger H, Schmitz G, Kirchheim R. Springer Ser Mater Sci 2003;50:271–320.
[21] Geber GP, Kirchheim R. Acta Mat 1997;45:2167–75.
[22] Schmuck C, Caron P, Hauet A, Blavette D. Philos Mag A 1997;76:527–42.
[23] Chambreland S, Walder A, Blavette D. Acta Metall 1988;36:3205–15.
[24] Miller MK. Micron 2001;32:757–64.
[25] Simmons JP, Wen Y, Shen C, Wang YZ. Mater Sci Eng, A 2004;A365:136–43.
[26] Wang J, Osawa M, Yokokawa T, Harada H, Enomoto M. Proc Int Symp Super 2004:933–40.
[27] Chu Z, Chen Z, Wang YX, Lu YL, Li YS. J Mater Sci Tech 2006;22:315–20.
[28] Wang Y, Banerjee D, Su CC, Khachaturyan AG. Acta Mat 1998;46:2983–3001.
[29] Wen YH, Wang B, Simmons JP, Wang Y. Acta Mat 2006;54:2087–99.
[30] Grafe U, Bottger B, Tiaden J, Fries SG. Scripta Mater 2000;42:1179–86.
[31] Wagner R, Kampmann R, Voorhees PW. Homogeneous second-phase precipitation. In: Kostorz G, editor. Phase transformations in materials. Weinheim: Wiley-VCH; 2001. p. 314.
[32] Mao Z, Sudbrack CK, Yoon KE, Martin G, Seidman DN. Nat Mater 2006;6:210–6.
[33] Schmuck C, Danoix F, Caron P, Hauet A, Blavette D. Appl Surf Sci 1996;94–5:273–9.
[34] Pareige-Schmuck C, Soisson F, Blavette D. Mater Sci Eng, A 1998;250:99–103.
[35] Pareige C, Soisson F, Martin G, Blavette D. Acta Mat 1999;47:1889–99.
[36] Sudbrack CK, Noebe RD, Seidman DN. Phys Rev B 2006;73. 212101/1–212101/4.
[37] Sudbrack CK, Yoon KE, Noebe RD, Seidman DN. Acta Mat 2006;54:3199–210.
[38] Sudbrack CK, Isheim D, Noebe RD, Jacobson NS, Seidman DN. Microsc Microanal 2004;10:355–65.
[39] Sudbrack CK, Ziebell TD, Noebe RD, Seidman DN. Acta Mat 2008;56:448–63.
[40] Sudbrack CK, Noebe RD, Seidman DN. Acta Mat 2007;55:119–30.
[41] Yoon KE, Sudbrack CK, Noebe RD, Seidman DN. Z Metall 2005;96:481–5.
[42] Yoon KE, Noebe RD, Seidman DN. Acta Mat 2007;55:1145–57.
[43] Yoon KE, Noebe RD, Seidman DN. Acta Mat 2007;55:1159–69.
[44] Mao Z, Sinnott SB, Martin G, Seidman DN, in preparation.
[45] Martin G. The Theories of unmixing kinetics of solid solutions. solid state phase transformation in metals and alloys. Orsay, France: Les Éditions de Physique; 1978. p. 337–406.
[46] Russell KC. Adv Colloid Interface Sci 1980;13:205–318.
[47] Kashchiev D. Nucleation: basic theory and applications. Oxford: Elsevier Science; 2000.
[48] Brechet Y, Martin G. CR Phys 2006;7:959–76.
[49] Robson JD. Acta Mat 2004;52:4669–76.
[50] Stowell MJ. Mater Sci Tech 2002;18:139–44.
[51] Aaronson HI, LeGoues FK. Metall Trans A 1992;23A:1915–45.
[52] Greenwood GW. Acta Metall 1956;4:243–8.
[53] Lifshitz IM, Slyozov VV. J Phys Chem Solids 1961;19:35–50.
[54] Wagner C. Z Electrochem 1961;65:581–91.
[55] Baldan A. J Mater Sci 2002;37:2171–202.
[56] Rowenhorst DJ, Kuang JP, Thornton K, Voorhees PW. Acta Mat 2006;54:2027–39.
[57] Voorhees PW. Annu Rev Mater Sci 1992;22:197–215.
[58] Ratke L, Voorhees PW. Growth and coarsening, ripening in material processing. Berlin: Springer-Verlag; 2002.
[59] Umantsev A, Olson GB. Scripta Metall Mater 1993;29:1135–40.
[60] Morral JE, Purdy GR. Scripta Metall Mater 1994;30:905–8.
[61] Kuehmann CJ, Voorhees PW. Metall Mater Trans, A 1996;27A:937–43.
[62] Blavette D, Deconihout B, Bostel A, Sarrau JM, Bouet M, Menand A. Rev Sci Instrum 1993;64:2911–9.
[63] Cerezo A, Godfrey TJ, Sijbrandij SJ, Smith GDW, Warren PJ. Rev Sci Instrum 1998;69:49–58.
[64] Bajikar SS, Larson DJ, Kelly TF, Camus PP. Ultramicroscopy 1996;65:119–29.
[65] Kelly TF, Camus PP, Larson DJ, Holzman LM, Bajikar SS. Ultramicroscopy 1996;62:29–42.
[66] Kelly TF, Larson DJ. Mater Charact 2000;44:59–85.
[67] Seidman DN. Annu Rev Mater Res 2007;37:127–58.
[68] Hellman OC, Vandenbroucke JA, Blatz du Rivage J, Seidman DN. Mater Sci Eng, A 2002;327:29–33.
[69] Hellman OC, Blatz du Rivage J, Seidman DN. Ultramicroscopy 2003;95:199–205.
[70] Hellman OC, Vandenbroucke JA, Rusing J, Isheim D, Seidman DN. Microsc Microanal 2000;6:437–44.
[71] Blavette D, Cadel E, Pareige C, Deconihout B, Caron P. Microsc Microanal 2007;13:464–83.
[72] Sundman B, Jansson B, Andersson JO. CALPHAD 1985;9:153–90.
[73] Saunders N. Proc Int Symp Super 1996:101–10.
[74] Dupin N, Ansara I, Sundman B. CALPHAD 2001;25:279–98.
[75] Parratt LG. Probability and experimental errors in science. New York: John Wiley; 1966.
[76] Wagner R, Kampmann R, Voorhees PW. Homogeneous second-phase precipitation. Weinheim: Wiley-VCH; 2001.
[77] Zener C. J Appl Phys 1949;20:950–3.
[78] Ham FS. J Appl Phys 1959;30:1518–25.
[79] Ardell AJ. Mater Sci Eng, A 1997;A238:108–20.
[80] Ardell AJ. Acta Metall 1968;16:511–6.
[81] Ardell AJ. Acta Metall 1967;15:1772–5.
[82] Marquis EA, Seidman DN. Acta Mat 2005;53:4259–68.
[83] Kresse G, Hafner J. Phys Rev B 1993;47:558–61.
[84] Kresse G, Furthmueller J. Phys Rev B 1996;54:11169–86.
[85] Kresse G, Furthmuller J. Comput Mater Sci 1996;6:15–50.
[86] Kresse G, Hafner J. Phys Rev B 1994;49:14251–69.
[87] Gleiter H, Hornbogen E. Z Metall 1967;58:157–63.
[88] Lupis CHP. Chemical thermodynamics of materials. New York: North-Holland; 1983.
[89] Christian JW. Theory of transformations in metals and alloys, part 1. Oxford: Pergamon Press; 1975.
[90] Prikhodko SV, Carnes JD, Isaak DG, Ardell AJ. Scripta Mater 1997;38:67–72.
[91] Stassis C, Kayser FX, Loong CK, Arch D. Phys Rev B 1981;24:3048–53.
[92] Eshelby JD. Proc Roy Soc A 1957;241:376–96.
[93] Karnesky RA, Martin G, Seidman DN, in preparation.

[94] Nembach E. Particle strengthening of metals and alloys. New York: John Wiley and Sons Inc.; 1997.
[95] Minamino Y, Jung SB, Yamane T, Hirao K. Metall Trans A 1992;23A:2783–90.
[96] Calderon HA, Voorhees PW, Murray JL, Kostorz G. Acta Metall Mater 1994;42:991–1000.
[97] Sundman B, Jansson B, Andersson JO. CALPHAD: Computer Coupling of Phase Diagrams and Thermochemistry 1985;9:153–90.